The Astrophysical Journal, 949:49 (17pp), 2023 June 1 https://doi.org/10.3847/1538-4357/acc5e1

A Chandra X-Ray Survey of Optically Selected Close Galaxy Pairs: Unexpectedly Low Occupation of Active Galactic Nuclei

Lin He[1,2], Meicun Hou[3], Zhiyuan Li[1,2], Shuai Feng[4,5], and Xin Liu[6,7]
[1] School of Astronomy and Space Science, Nanjing University, Nanjing 210023, People's Republic of China
[2] Key Laboratory of Modern Astronomy and Astrophysics (Nanjing University), Ministry of Education, Nanjing 210023, People's Republic of China
[3] Kavli Institute for Astronomy and Astrophysics, Peking University, Beijing 100871, People's Republic of China; houmc@pku.edu.cn
[4] College of Physics, Hebei Normal University, 20 South Erhuan Road, Shijiazhuang, 050024, People's Republic of China
[5] Hebei Key Laboratory of Photophysics Research and Application, 050024 Shijiazhuang, People's Republic of China
[6] Department of Astronomy, University of Illinois at Urbana-Champaign, Urbana, IL 61801, USA
[7] National Center for Supercomputing Applications, University of Illinois at Urbana-Champaign, 605 East Springfield Avenue, Champaign, IL 61820, USA
Received 2022 November 10; revised 2023 February 23; accepted 2023 March 14; published 2023 May 26

Abstract

High-resolution X-ray observations offer a unique tool for probing the still-elusive connection between galaxy mergers and active galactic nuclei (AGNs). We present an analysis of nuclear X-ray emission in an optically selected sample of 92 close galaxy pairs (with projected separations $\lesssim$20 kpc and line-of-sight velocity offsets $<$500 km s^{-1}) at low redshift ($\bar{z} \sim 0.07$), based on archival Chandra observations. The parent sample of galaxy pairs is constructed without imposing an optical classification of nuclear activity, thus it is largely free of selection effect for or against the presence of an AGN. Nor is this sample biased for or against gas-rich mergers. An X-ray source is detected in 70 of the 184 nuclei, giving a detection rate of $38\%^{+5\%}_{-5\%}$, down to a 0.5–8 keV limiting luminosity of $\lesssim 10^{40}$ erg s^{-1}. The detected and undetected nuclei show no systematic difference in their host galaxy properties such as galaxy morphology, stellar mass, and stellar velocity dispersion. When potential contamination from star formation is avoided (i.e., $L_{2-10\,\mathrm{keV}} > 10^{41}$ erg s^{-1}), the detection rate becomes $18\%^{+3\%}_{-3\%}$ (32/184), which shows no excess compared to the X-ray detection rate of a comparison sample of optically classified single AGNs. The fraction of pairs containing dual AGN is only $2\%^{+2\%}_{-2\%}$. Moreover, most nuclei at the smallest projected separations probed by our sample (a few kiloparsecs) have an unexpectedly low apparent X-ray luminosity and Eddington ratio, which cannot be solely explained by circumnuclear obscuration. These findings suggest that close galaxy interaction is not a sufficient condition for triggering a high level of AGN activity.

Unified Astronomy Thesaurus concepts: Galaxy nuclei (609); Interacting galaxies (802); Galaxy mergers (608); X-ray active galactic nuclei (2035)

Supporting material: machine-readable tables

1. Introduction

It is a generic prediction of the standard paradigm of hierarchical structure formation that most galaxies frequently interact with other galaxies during their lifetime. When the two interacting galaxies are gravitationally bound, their ultimate fate is to merge, eventually forming a more massive galaxy. In the course of galaxy mergers, tidal force and ram pressure act to significantly redistribute the stellar and gaseous contents of the interacting pair (Toomre & Toomre 1972; Barnes & Hernquist 1992). It is theoretically predicted and has been demonstrated by numerical simulations (e.g., Di Matteo et al. 2005) that upon close passages, gravitational torques drive gas inflows to the center of one or both galaxies, potentially triggering nuclear star formation and active galactic nuclei (AGNs). A physical consequence of this scenario is the prevalence of AGN pairs in (major) galaxy mergers, which involve two SMBHs with simultaneous active accretion. Specifically, "dual AGNs," AGN pairs with a separation $\lesssim$10 kpc in projection, are generally expected at the intermediate-to-late stage of mergers (see recent review by De Rosa et al. 2019). This is a crucial phase during which the SMBH(s) can significantly grow its mass, preceding the formation of an SMBH binary and their ultimate merger (Merritt & Milosavljević 2005).

As observational validation of the above scenario, a number of systematic searches for dual AGN candidates have been conducted over the past decade, primarily in the optical band, thanks to wide-field, homogeneous spectroscopic surveys such as the Sloan Digital Sky Survey (SDSS). In particular, the search for galactic nuclei with double-peaked narrow emission lines (e.g., [O III]; Wang et al. 2009; Liu et al. 2010) aims at tight AGN pairs (typically 1–10 kpc in separation, but even less) that pertain to the late stage of merger, whereas the search for resolved pairs of galactic nuclei both showing the optical emission-line characteristics of Seyfert or Low Ionization Nuclear Emission-line Region (LINER) covers larger projected separations up to ~100 kpc (Liu et al. 2011, hereafter L11). Confirmation of the AGN nature in these optically selected candidates, however, often require follow-up observations in the X-ray and/or radio bands (Comerford et al. 2011; Silverman et al. 2011; Teng et al. 2012; Liu et al. 2013; Fu et al. 2015a, 2015b; Brightman et al. 2018; Gross et al. 2019; Hou et al. 2019; Foord et al. 2020), which are generally thought to trace immediate radiation from the SMBH (more precisely, from the accretion disk, corona, and/or jets) and tend to be more immune to circumnuclear obscuration. Infrared observations have also played an effective role in revealing dual

AGNs, especially in gas-rich merging systems, which tend to select highly obscured AGNs (Satyapal et al. 2014, 2017; Pfeifle et al. 2019). An alternative approach (Koss et al. 2012) starts with a hard X-ray ($\gtrsim$10 keV) AGN detected in the Swift/BAT survey and tries to associate it with another AGN in a companion galaxy within a projected distance of 100 kpc, if it exists. This approach, however, inevitably introduced selection bias toward X-ray-luminous AGNs due to the moderate sensitivity of Swift/BAT. Nevertheless, these approaches have achieved a certain degree of success, revealing a growing number of AGN pairs and dual AGNs.

Clearly, having a sizable and unbiased sample of genuine dual AGNs is crucial for a thorough understanding of the causality between galaxy mergers and AGN triggering. Recently, Hou et al. (2020, hereafter H20) carried out a systematic search for X-ray-emitting AGN pairs, using archival Chandra observations and based on the Liu et al. (2011) sample of $\sim 10^3$ optically selected AGN pairs at low redshift (with a median redshift $\bar{z} \sim 0.1$). Thanks to the superb angular resolution of Chandra, unattainable from any other X-ray facility, one can unambiguously resolve and localize the putative AGN even in close pairs. More importantly, the typical sensitivity of Chandra observations used by Hou et al. (2020) is sufficient to probe low-luminosity AGNs (i.e., weakly accreting SMBHs) down to a limiting 2–10 keV X-ray luminosity of $L_{2-10} \sim 10^{40}$ erg s^{-1}, which is necessary for a complete census of nuclear activity.

Among 67 pairs of the optically selected AGN candidates with useful Chandra data, Hou et al. (2020) found that 21 pairs show significant X-ray emission from both nuclei (i.e., probable AGN pairs), with an additional 36 pairs having only one of the two nuclei detected. The X-ray detection rate of all 134 nuclei, $58\% \pm 7\%$ (1σ Poisson errors), is significantly higher than that ($17\% \pm 4\%$) of a comparison sample of star-forming galaxy pairs, classified also based on optical emission-line ratios. Moreover, interesting trends were revealed for the mean X-ray luminosity as a function of the projected separation, $r_{\rm p}$, which is taken as a proxy for the merger phase, where larger (smaller) $r_{\rm p}$ represents the earlier (later) stage of a merger. First, L_{2-10} increases with decreasing projected separation in AGN pairs at $r_{\rm p} \gtrsim 20$ kpc, suggesting enhanced SMBH accretion even in early-stage mergers, perhaps related to the first pericentric passage of the two galaxies. Second and unexpectedly, L_{2-10} decreases (rather than increases) with decreasing $r_{\rm p}$ at $r_{\rm p} \lesssim 10$ kpc, which appears contradicting with the intuitive expectation that tidal-force-driven gas inflows become more and more prevalent as mergers proceed. Despite the small number statistics, Hou et al. (2020) proposed two physical explanations for this latter behavior: (i) merger-induced gas inflows become so strong that an enhanced central concentration of cold gas heavily obscures even the hard (2–10 keV) X-rays; (ii) AGN feedback triggered by the first pericentric passage acts to expel gas from the nuclear region and consequently suppress or even halt SMBH accretion. The latter possibility is of particular interest, potentially offering insight into the still-elusive processes of SMBH feeding and feedback during an indispensable stage of galaxy evolution.

Extending the study of Hou et al. (2020), in this work we use archival Chandra observations to survey the nuclear X-ray emission from a new sample of close galaxies pairs. These close galaxies pairs are selected from optical spectroscopic surveys (see Section 2 for details), but they are not subject to a pre-selection of optical AGN characteristics as applied in Hou et al. (2020), thus allowing for an unbiased view of AGN activity through their nuclear X-ray emission. This paper is structured as follows. Section 2 describes the construction of a new sample of close galaxy pairs with archival Chandra observations. Data analysis toward detection and characterization of the nuclei are detailed in Section 3. Section 4 presents the results, including the properties and statistics of the X-ray detected nuclei and a reexamination of the behavior of L_{2-10} as a function of $r_{\rm p}$. Section 5 summarizes the study and address most significant implications. Throughout this work, we assume a concordance cosmology with $\Omega_m = 0.3$, $\Omega_\Lambda = 0.7$, and $H_0 = 70$ km s^{-1} Mpc^{-1}. Errors are quoted at 1σ confidence level unless otherwise stated.

2. The Sample of Close Galaxy Pairs

In this work, we construct a new sample of close galaxy pairs based on the parent sample of galaxy pairs recently presented by Feng et al. (2019, hereafter F19). The F19 sample itself was extracted from the SDSS DR7 (Abazajian et al. 2009) photometric galaxy catalog, with $\sim$95% of the cataloged galaxies having an available spectroscopic redshift, which was primarily from SDSS and supplemented by LAMOST (Luo et al. 2015; Shen et al. 2016), GAMA (Baldry et al. 2018), and other spectroscopic surveys (see detailed description in Feng et al. 2019). A close galaxy pair was selected if the two member galaxies have a line-of-sight velocity offset $\Delta v < 500$ km s^{-1} and a projected separation $r_{\rm p} \lesssim 20$ kpc. We also required that each galaxy has only one neighbor galaxy with a similar redshift within a projected separation of 100 kpc and a velocity offset of 500 km s^{-1}, to minimize environmental effects typical of compact groups or clusters. Contrary to Feng et al. (2019), who focused on pairs with $r_{\rm p} > 10\ h^{-1}$ kpc, we impose no lower limit on $r_{\rm p}$. However, due to the resolution limit of the optical surveys ($\sim 1''$), the Feng et al. (2019) sample still suffers from incompleteness for the most closely separated pairs (i.e., $\lesssim$1 kpc).

We thus have a preliminary list of 3337 close galaxy pairs. A comparison with the Liu et al. (2011) sample of optically selected AGN pairs shows that the two samples have 130 common pairs, whereas 3207 pairs are in the Feng et al. (2019) sample but not in the Liu et al. (2011) sample. This difference partly stems from the fact that the Liu et al. (2011) sample, which was primarily based on SDSS DR7 spectroscopic redshifts, suffers from the restriction of SDSS fiber collision and thus is missing closely separated galaxy pairs. The Feng et al. (2019) sample was exactly designed to overcome this incompleteness, thereby significantly increasing the number of close galaxy pairs. Moreover, the Liu et al. (2011) sample required both galaxies in a pair to have a Seyfert or LINER classification based on the optical emission-line diagnostics, whereas the Feng et al. (2019) sample only required a spectroscopic redshift based primarily on stellar continuum, thus it, in principle, minimizes the selection bias for or against AGN activity in closely interacting galaxies (though see Section 4.4 for potential bias for the most luminous AGNs in a few Chandra observations), as well as selection bias for or against gas-rich mergers.

We cross-matched the Feng et al. (2019) sample with the Chandra X-ray data archive to select pairs with observations taken with the Advanced CCD Imaging Spectrometer (ACIS) and publicly available as of June 2022. Similar to Hou et al. (2020), we requested that both galactic nuclei in a pair fall

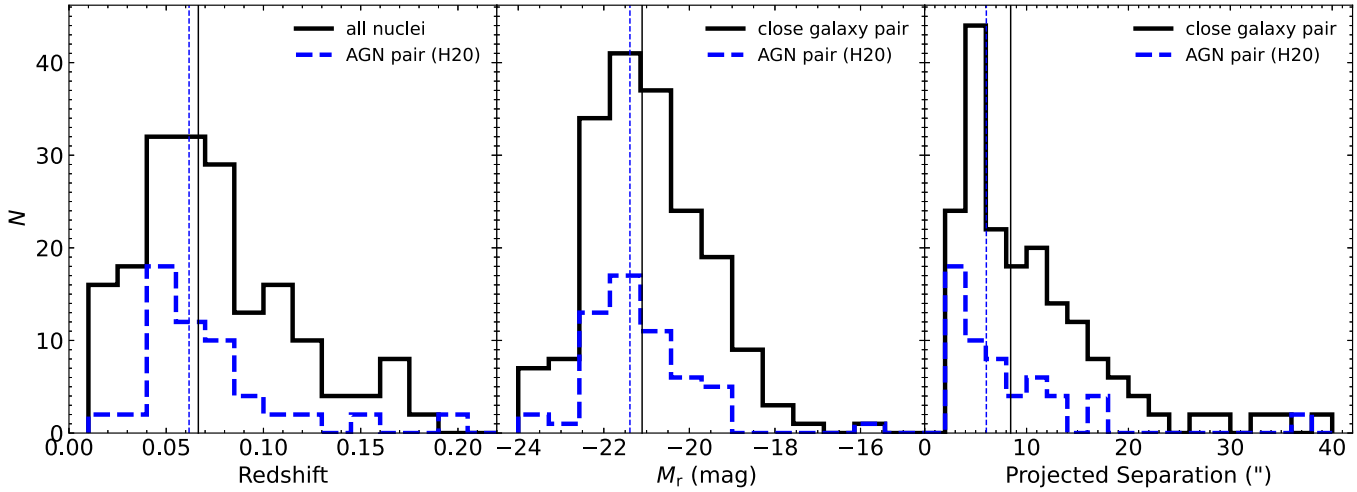

Figure 1. Redshift (left panel), *r*-band absolute magnitude (middle panel), and projected angular separation (right panel) distributions of the close galaxy pairs studied in this work (black solid histogram), in comparison with the close AGN pairs (blue dashed) in Hou et al. (2020). The vertical lines mark the median value of the individual samples.

within the ACIS field of view and within 8′ from the aimpoint, to ensure the feasibility of source detection and photometry. We further visually inspected the SDSS to filter several spurious galaxy pairs, which are most likely compact star-forming clusters/complexes that mimicked a second galactic nucleus. Our final sample consists of 92 optically and X-ray selected galaxy pairs, which have r_p ranging from 3.0 to 19.7 kpc. This small fraction (92/3337) reflects the empirical rule that on average only a few percent of randomly selected sky targets would fall on a Chandra/ACIS footprint. Basic information of these galaxy pairs are given in Table 1.

Our sample is an extension of the AGN pairs and SFG pairs studied by Hou et al. (2020). The Hou et al. (2020) AGN pairs, selected from the parent sample of Liu et al. (2011), cover a wider range of projected separations ($r_p < 100$ kpc) and have both nuclei classified as an AGN based on the optical emission-line diagnostics. Hou et al. (2020) also constructed a comparison sample of SFG pairs (i.e., both nuclei having the optical emission-line diagnostics of star formation). Considering only the close pairs (i.e., those with $r_p < 20$ kpc) in Hou et al. (2020), there are 28 AGN pairs and 12 SFG pairs. For clarity, hereafter we refer to AGN pairs or SFG pairs of Hou et al. (2020) as those pairs with $r_p < 20$ kpc only, unless otherwise stated. With our new sample, which presumes no distinction between optically classified AGN and SFG, the total number of close galaxy pairs with both Chandra and optical spectroscopic observations is now more than doubled. We note that the new sample includes 17 AGN pairs and 1 SFG pair in Hou et al. (2020). These pairs are kept in the following analysis, but caution is taken not to double-count them when an analysis also involves those pairs from Hou et al. (2020). There also exist some pairs that belong to Hou et al. (2020) but are not included in the new sample. This is mainly due to the fact that the Liu et al. (2011) sample did not impose the requirement on the absence of a third galaxy within 100 kpc and also included some pairs that are not part of the parent galaxy sample of Feng et al. (2019).

Figure 1 compares the redshift (left panel) and SDSS *r*-band absolute magnitude (M_r; middle panel) distributions of the current sample with those of the AGN pairs in Hou et al. (2020). The current sample has a median redshift $\bar{z} = 0.067$ and a median *r*-band absolute magnitude $\bar{M}_r = -21.1$ mag, while the close AGN pairs have a similar $\bar{z} = 0.062$ and $\bar{M}_r = -21.4$ mag.

3. Data Analysis

3.1. Chandra Data Preparation

The Chandra/ACIS data were reprocessed following the standard procedure, using CIAO v4.13 with the calibration files CALDB v4.9.5.[8] Among the 92 galaxy pairs in the current sample, 78 pairs have only one observation, while the the other 14 pairs have been observed more than one time, for which we combined all available observations.

Following the procedures in Hou et al. (2020), for each observation we produced counts, exposure, and point-spread function (PSF) maps on the natal pixel scale of 0.″492 in the 0.5–2 (*S*), 2–8 (*H*), and 0.5–8 (*F*) keV band. The exposure maps and the PSF maps were weighted by a fiducial incident spectrum, which is an absorbed power-law with a photon index of 1.7 (a median value for AGN, see Winter et al. 2009) and absorption column densities $N_H = 10^{22}$ cm^{-2} for the *H* band and $N_H = 10^{21}$ cm^{-2} for the *S* band.

For targets with multiple observations, the counts, exposure, and PSF maps of individual observations were reprojected to a common tangential point after calibrating their relative astrometry, to produce combined images that maximize the source detection sensitivity. Only the I0, I1, I2, and I3 CCDs for the ACIS-I observations and the S2 and S3 CCDs for the ACIS-S observations were included at this step. We have examined the light curves of each observation and filtered time intervals contaminated by significant particle flares, if any. The effective exposure time of each target pair ranged from 1.1 to 240.1 ks, with a median value of 13.7 ks.

3.2. X-Ray Counterparts and Photometry

We followed the procedures detailed in Hou et al. (2020) to search for X-ray counterparts of the optical nuclei in our close galaxy pairs. We first performed source detection in the 0.5–2, 2–8, and 0.5–8 keV bands for each galaxy pair using the CIAO tool *wavdetect*, with the 50% enclosed count fraction (ECF)

[8] http://cxc.harvard.edu/ciao/

Table 1
Information of Close Galaxy Pairs with Chandra Observation

Name (1)	R.A. (2)	Decl. (3)	z (4)	r_p (5)	log M_* (6)	SFR (7)	log M_{BH} (8)	log $L_{X,lim}$ (9)	Flag (10)
J102700.40+174901.0	156.75167	17.81694	0.0665	3.0	10.9	$1.09^{+3.04}_{-0.97}$	7.4	40.17	0
J102700.56+174900.3	156.75233	17.81675	0.0666	3.0	⋯	$12.86^{+29.44}_{-9.38}$	⋯	40.17	1
J085837.53+182221.6	134.65637	18.37267	0.0587	3.3	10.4	$3.55^{+8.31}_{-2.62}$	7.5	40.39	1
J085837.68+182223.4	134.65700	18.37317	0.0589	3.3	11.1	$3.46^{+9.05}_{-2.88}$	7.7	40.39	1
J105842.44+314457.6	164.67683	31.74933	0.0728	4.1	10.0	$1.95^{+2.73}_{-1.19}$	6.1	40.71	1
J105842.58+314459.8	164.67742	31.74994	0.0723	4.1	10.9	$2.44^{+5.33}_{-1.75}$	7.5	40.70	1
J002208.69+002200.5	5.53621	0.36681	0.0710	4.2	11.0	$0.02^{+0.15}_{-0.02}$	7.8	40.41	1
J002208.83+002202.8	5.53679	0.36744	0.0707	4.2	11.2	$0.02^{+0.14}_{-0.02}$	8.1	40.44	1
J133031.75−003611.9	202.63229	−0.60331	0.0542	4.4	8.8	$0.35^{+0.49}_{-0.21}$	⋯	40.44	0
J133032.00−003613.5	202.63333	−0.60375	0.0542	4.4	10.7	$3.98^{+6.69}_{-2.57}$	7.4	40.44	1
J141447.15−000013.3	213.69646	−0.00369	0.0475	4.9	10.5	$0.23^{+0.71}_{-0.22}$	6.9	40.04	1
J141447.48−000011.3	213.69783	−0.00314	0.0474	4.9	10.2	$3.54^{+4.94}_{-2.12}$	6.0	40.03	1
J235654.30−101605.4	359.22628	−10.26817	0.0739	4.9	⋯	⋯	⋯	41.10	1
J235654.49−101607.4	359.22708	−10.26875	0.0732	4.9	9.3	$2.47^{+0.23}_{-0.17}$	⋯	41.03	0
J091931.14+333852.1	139.87977	33.64782	0.0237	5.1	8.5	$0.13^{+0.01}_{-0.03}$	⋯	40.70	0
J091930.30+333854.4	139.87628	33.64845	0.0237	5.1	⋯	⋯	⋯	40.78	0
J093529.56+033923.1	143.87320	3.65644	0.0463	5.4	⋯	⋯	⋯	41.52	0
J093529.77+033918.1	143.87408	3.65505	0.0464	5.4	10.0	$0.81^{+0.11}_{-0.13}$	⋯	41.55	0
J122814.15+442711.7	187.05896	44.45325	0.0233	5.5	10.7	$0.06^{+0.21}_{-0.06}$	6.9	41.06	1
J122815.23+442711.3	187.06348	44.45314	0.0229	5.5	⋯	⋯	⋯	41.01	1
J112648.50+351503.2	171.70212	35.25089	0.0322	5.9	⋯	⋯	⋯	40.02	1
J112648.65+351454.2	171.70274	35.24839	0.0321	5.9	10.0	$2.03^{+0.18}_{-0.39}$	6.7	40.01	1
J090025.61+390349.2	135.10672	39.06369	0.0583	5.9	9.9	$0.43^{+0.13}_{-0.07}$	⋯	40.48	0
J090025.37+390353.7	135.10572	39.06492	0.0582	5.9	10.1	$7.22^{+9.32}_{-4.22}$	8.3	40.48	1
J151806.13+424445.0	229.52558	42.74585	0.0403	6.2	10.8	$50.00^{+74.29}_{-31.82}$	8.4	40.13	1
J151806.37+424438.1	229.52664	42.74387	0.0407	6.2	⋯	⋯	⋯	40.14	1
J104518.04+351913.1	161.32520	35.32032	0.0676	6.2	10.6	$28.86^{+4.67}_{-6.07}$	7.7	40.30	1
J104518.43+351913.5	161.32682	35.32041	0.0674	6.2	10.6	$27.08^{+38.08}_{-16.33}$	7.0	40.30	1
J090332.77+011236.3	135.88657	1.21009	0.0580	6.3	10.2	$0.17^{+0.46}_{-0.15}$	6.7	40.33	0
J090332.99+011231.7	135.88747	1.20881	0.0579	6.3	9.7	$0.09^{+0.23}_{-0.07}$	⋯	40.33	0
J133817.27+481632.3	204.57196	48.27564	0.0278	6.4	10.0	$5.48^{+7.89}_{-3.33}$	7.8	40.12	1
J133817.77+481641.1	204.57404	48.27808	0.0277	6.4	10.6	$2.84^{+3.66}_{-1.66}$	8.1	40.13	1
J114753.63+094552.0	176.97346	9.76444	0.0951	6.6	10.3	$8.63^{+14.39}_{-5.58}$	8.6	40.93	1
J114753.68+094555.6	176.97367	9.76544	0.0966	6.6	11.0	$1.10^{+1.56}_{-0.63}$	7.7	40.95	0
J093634.03+232627.0	144.14185	23.44083	0.0284	6.8	10.8	$0.00^{+0.03}_{-0.00}$	7.8	40.51	1
J093633.93+232638.7	144.14144	23.44411	0.0283	6.8	10.5	$1.83^{+0.39}_{-0.42}$	6.9	40.50	0
J123257.15+091756.1	188.23816	9.29892	0.1048	7.3	11.3	$0.03^{+0.20}_{-0.03}$	8.2	41.76	0
J123257.38+091757.7	188.23912	9.29939	0.1049	7.3	⋯	⋯	⋯	41.76	0
J135853.78+280346.7	209.72413	28.06300	0.0866	7.4	10.1	$0.12^{+0.34}_{-0.11}$	⋯	41.48	0
J135853.66+280342.5	209.72362	28.06182	0.0868	7.4	⋯	⋯	⋯	41.56	0
J084113.09+322459.6	130.30455	32.41657	0.0684	7.7	⋯	⋯	⋯	39.92	1
J084112.79+322455.1	130.30329	32.41533	0.0696	7.7	10.3	$0.13^{+0.17}_{-0.07}$	8.0	39.94	0
J140737.16+442856.2	211.90487	44.48229	0.1429	7.7	10.8	$0.80^{+2.02}_{-0.62}$	7.0	41.14	0
J140737.43+442855.1	211.90600	44.48200	0.1430	7.7	⋯	⋯	⋯	41.14	1
J084135.08+010156.1	130.39619	1.03228	0.1106	7.8	10.5	$5.88^{+7.55}_{-3.44}$	⋯	40.74	1
J084134.87+010153.9	130.39532	1.03165	0.1105	7.8	⋯	⋯	⋯	40.74	0
J230010.24−000533.9	345.04269	−0.09276	0.1798	7.9	11.5	$0.06^{+0.41}_{-0.06}$	8.9	41.33	0
J230010.17−000531.5	345.04239	−0.09211	0.1797	7.9	11.8	$0.09^{+0.69}_{-0.09}$	8.8	41.33	1
J112536.15+542257.2	171.40067	54.38264	0.0207	7.9	⋯	⋯	⋯	39.94	1
J112535.23+542314.4	171.39682	54.38741	0.0206	7.9	7.1	$0.02^{+0.03}_{-0.01}$	⋯	39.87	0
J121247.04+070821.6	183.19604	7.13933	0.1362	8.3	⋯	$0.72^{+0.95}_{-0.39}$	⋯	42.44	0
J121246.84+070823.0	183.19517	7.13975	0.1367	8.3	⋯	⋯	⋯	42.44	0
J102229.47+383538.4	155.62280	38.59401	0.0519	8.6	10.9	$0.02^{+0.09}_{-0.01}$	7.6	40.35	0
J102229.95+383544.7	155.62480	38.59577	0.0523	8.6	9.6	$0.02^{+0.02}_{-0.01}$	⋯	40.35	0
J004343.80+010216.9	10.93251	1.03805	0.1069	8.8	10.4	$0.03^{+0.18}_{-0.03}$	7.7	41.98	0
J004344.07+010215.1	10.93365	1.03754	0.1070	8.8	10.5	$2.95^{+0.87}_{-0.43}$	6.9	41.96	0
J083817.59+305453.5	129.57329	30.91486	0.0478	8.8	10.7	$2.62^{+5.73}_{-1.88}$	7.0	40.88	1
J083817.95+305501.1	129.57479	30.91697	0.0481	8.8	11.2	$0.05^{+0.28}_{-0.04}$	7.3	40.89	0

Table 1
(Continued)

Name (1)	R.A. (2)	Decl. (3)	z (4)	r_p (5)	log M_* (6)	SFR (7)	log M_{BH} (8)	log $L_{X,lim}$ (9)	Flag (10)
J110713.23+650606.6	166.80511	65.10192	0.0328	8.8	11.2	$0.03^{+0.20}_{-0.03}$	8.1	40.62	1
J110713.49+650553.2	166.80622	65.09819	0.0319	8.8	…	…	…	40.53	1
J090714.45+520343.4	136.81021	52.06206	0.0596	8.9	10.6	$0.59^{+1.61}_{-0.52}$	7.7	40.54	1
J090714.61+520350.7	136.81087	52.06408	0.0602	8.9	10.3	$1.28^{+2.95}_{-0.94}$	7.0	40.55	1
J145309.42+215404.4	223.28929	21.90123	0.1169	9.2	11.0	$0.03^{+0.18}_{-0.03}$	8.3	42.18	0
J145309.62+215407.8	223.29010	21.90220	0.1155	9.2	10.8	$0.01^{+0.09}_{-0.01}$	7.9	42.13	0
J111828.42−003302.7	169.61845	−0.55077	0.1001	9.3	10.8	$0.03^{+0.18}_{-0.03}$	7.4	41.62	0
J111828.41−003307.8	169.61842	−0.55216	0.1003	9.3	10.3	$0.60^{+0.22}_{-0.16}$	6.5	41.62	0
J134736.41+173404.7	206.90171	17.56797	0.0447	9.3	9.4	$0.30^{+0.41}_{-0.18}$	…	41.17	1
J134737.11+173404.1	206.90462	17.56781	0.0450	9.3	10.5	$0.13^{+0.35}_{-0.11}$	6.7	41.18	0
J142445.68+333749.4	216.19036	33.63039	0.0710	9.5	…	…	…	41.48	0
J142445.86+333742.7	216.19111	33.62855	0.0718	9.5	10.5	$2.47^{+0.59}_{-0.41}$	…	41.50	0
J000249.07+004504.8	0.70446	0.75133	0.0868	9.5	11.2	$0.16^{+0.97}_{-0.15}$	8.6	41.60	1
J000249.44+004506.7	0.70600	0.75186	0.0865	9.5	10.9	$0.01^{+0.09}_{-0.01}$	7.8	41.60	0
J094543.54+094901.5	146.43146	9.81709	0.1564	9.6	…	…	…	41.74	1
J094543.78+094901.2	146.43245	9.81700	0.1566	9.6	11.2	$25.98^{+36.44}_{-14.72}$	7.5	41.64	0
J143106.40+253800.0	217.77668	25.63335	0.0964	9.7	10.9	$0.02^{+0.11}_{-0.02}$	8.1	41.69	0
J143106.79+253801.3	217.77832	25.63370	0.0961	9.7	…	…	…	41.69	0
J085953.33+131055.3	134.97224	13.18205	0.0308	9.7	10.6	$0.44^{+2.10}_{-0.42}$	6.9	39.98	1
J085952.51+131044.3	134.96882	13.17900	0.0297	9.7	10.1	$0.01^{+0.01}_{-0.01}$	5.8	39.94	0
J123515.49+122909.0	188.81454	12.48585	0.0485	9.9	10.3	$0.01^{+0.08}_{-0.01}$	6.1	40.06	1
J123516.05+122915.4	188.81688	12.48763	0.0488	9.9	9.5	$0.15^{+0.03}_{-0.03}$	…	40.06	0
J161758.52+345439.9	244.49387	34.91109	0.1497	10.0	…	…	…	41.97	1
J161758.62+345436.3	244.49426	34.91007	0.1492	10.0	…	…	…	41.96	0
J125253.91−031811.0	193.22466	−3.30309	0.0863	10.3	10.6	$0.07^{+0.31}_{-0.06}$	7.1	41.88	0
J125254.33−031812.1	193.22640	−3.30338	0.0862	10.3	…	…	…	41.88	0
J121514.42+130604.5	183.81009	13.10126	0.1227	10.3	11.1	$0.03^{+0.17}_{-0.03}$	8.4	41.71	0
J121514.17+130601.5	183.80906	13.10043	0.1242	10.3	10.9	$0.08^{+0.33}_{-0.07}$	7.4	41.76	0
J095749.15+050638.3	149.45481	5.11066	0.1217	10.7	11.1	$0.04^{+0.26}_{-0.04}$	7.9	41.49	1
J095748.95+050642.2	149.45399	5.11174	0.1221	10.7	…	…	…	41.50	0
J123637.31+163351.8	189.15549	16.56441	0.0728	10.7	10.8	$0.01^{+0.04}_{-0.01}$	6.9	40.62	0
J123637.50+163344.6	189.15627	16.56239	0.0733	10.7	11.1	$0.02^{+0.11}_{-0.02}$	8.5	40.66	1
J114608.29−010709.8	176.53458	−1.11940	0.1189	11.2	11.1	$0.05^{+0.34}_{-0.05}$	8.2	41.28	0
J114608.19−010714.8	176.53414	−1.12078	0.1190	11.2	…	…	…	41.28	0
J151110.35+054851.7	227.79314	5.81437	0.0799	11.8	…	…	…	40.43	0
J151109.85+054849.3	227.79105	5.81370	0.0803	11.8	10.3	$0.01^{+0.04}_{-0.01}$	6.6	40.45	0
J124545.20+010447.5	191.43836	1.07987	0.1068	11.9	11.3	$12.39^{+21.73}_{-8.11}$	8.1	41.35	1
J124545.13+010453.4	191.43807	1.08153	0.1064	11.9	10.9	$0.03^{+0.16}_{-0.02}$	7.1	41.34	0
J094130.00+412302.0	145.37504	41.38390	0.0174	12.1	…	…	…	39.76	0
J094132.00+412235.5	145.38339	41.37656	0.0172	12.1	8.6	$0.01^{+0.01}_{-0.00}$	…	39.73	0
J090134.48+180942.9	135.39368	18.16195	0.0665	12.2	10.8	$0.01^{+0.09}_{-0.01}$	7.3	41.39	1
J090135.15+180941.7	135.39646	18.16159	0.0665	12.2	9.7	$0.07^{+0.05}_{-0.02}$	…	41.63	0
J105622.07+421807.8	164.09208	42.30219	0.0775	12.3	…	…	…	39.90	1
J105622.82+421809.7	164.09518	42.30267	0.0776	12.3	10.3	$0.02^{+0.08}_{-0.02}$	…	39.90	0
J132924.60+114816.5	202.35253	11.80459	0.0222	12.4	…	…	…	39.28	0
J132924.25+114749.3	202.35108	11.79703	0.0216	12.4	10.5	$1.31^{+0.57}_{-0.41}$	6.4	39.25	1
J111136.07+574952.4	167.90019	57.83131	0.0472	12.5	…	…	…	41.11	0
J111134.88+574942.8	167.89524	57.82866	0.0465	12.5	9.9	$0.46^{+0.19}_{-0.13}$	…	41.27	0
J135429.06+132757.3	208.62108	13.46592	0.0633	12.5	10.1	$0.04^{+0.12}_{-0.04}$	7.0	40.82	1
J135429.18+132807.4	208.62158	13.46872	0.0634	12.5	10.7	$0.64^{+1.66}_{-0.52}$	7.0	40.82	0
J125725.84+273246.0	194.35769	27.54613	0.0186	12.5	10.2	$0.00^{+0.02}_{-0.00}$	7.6	39.23	1
J125723.56+273259.7	194.34822	27.54993	0.0201	12.5	9.0	$0.00^{+0.00}_{-0.00}$	…	39.32	0
J011448.67−002946.0	18.70281	−0.49612	0.0338	12.6	…	…	…	40.18	1
J011449.81−002943.6	18.70760	−0.49542	0.0349	12.6	…	$0.16^{+0.03}_{-0.03}$	…	40.15	0
J145051.50+050652.1	222.71458	5.11448	0.0275	12.6	11.0	$3.24^{+4.45}_{-1.94}$	7.5	39.92	1
J145050.63+050710.8	222.71097	5.11968	0.0282	12.6	…	…	…	39.94	1
J075311.87+123749.1	118.29946	12.63031	0.0298	12.9	…	…	…	39.87	0
J075313.34+123749.1	118.30561	12.63031	0.0294	12.9	8.3	$0.23^{+0.01}_{-0.04}$	…	39.86	0

Table 1
(Continued)

Name (1)	R.A. (2)	Decl. (3)	z (4)	r_p (5)	log M_* (6)	SFR (7)	log M_{BH} (8)	log $L_{X,lim}$ (9)	Flag (10)
J134844.49+271044.7	207.18540	27.17911	0.0599	12.9	⋯	⋯	⋯	40.23	1
J134844.48+271055.9	207.18535	27.18220	0.0596	12.9	9.9	$0.02^{+0.08}_{-0.02}$	⋯	40.23	0
J141958.98+060320.1	214.99577	6.05560	0.0473	13.4	⋯	⋯	⋯	40.64	0
J141959.06+060305.7	214.99610	6.05161	0.0472	13.4	9.5	$0.02^{+0.02}_{-0.01}$	⋯	40.63	0
J090005.15+391952.2	135.02159	39.33120	0.0959	14.0	11.3	$0.03^{+0.20}_{-0.03}$	8.2	41.62	1
J090005.69+391947.4	135.02384	39.32988	0.0968	14.0	⋯	⋯	⋯	41.64	0
J125315.57−031030.2	193.31490	−3.17507	0.0845	14.1	10.4	$1.52^{+2.23}_{-0.93}$	6.1	41.71	0
J125315.99−031036.4	193.31665	−3.17680	0.0852	14.1	10.3	$0.74^{+0.43}_{-0.26}$	⋯	41.66	1
J135225.64+142919.3	208.10683	14.48869	0.0415	14.1	10.7	$0.01^{+0.07}_{-0.01}$	7.4	40.83	0
J135226.65+142927.5	208.11104	14.49097	0.0406	14.1	11.2	$3.74^{+7.98}_{-2.65}$	7.8	40.81	0
J141807.91+073232.5	214.53297	7.54237	0.0239	14.2	⋯	⋯	⋯	40.28	0
J141805.96+073226.7	214.52486	7.54077	0.0234	14.2	9.3	$0.00^{+0.02}_{-0.00}$	⋯	40.27	0
J125400.79+462752.4	193.50335	46.46458	0.0610	14.5	⋯	⋯	⋯	41.43	0
J125359.62+462750.2	193.49846	46.46397	0.0614	14.5	10.3	$0.68^{+2.06}_{-0.63}$	5.8	41.37	1
J163026.65+243640.2	247.61105	24.61118	0.0623	14.7	10.8	$0.01^{+0.07}_{-0.01}$	7.4	40.87	0
J163026.85+243652.1	247.61189	24.61449	0.0619	14.7	10.0	$0.01^{+0.04}_{-0.01}$	⋯	40.87	0
J080133.07+141341.6	120.39136	14.22618	0.0538	14.8	9.3	$0.22^{+0.03}_{-0.03}$	⋯	40.00	0
J080133.94+141334.0	120.38784	14.22821	0.0529	14.8	9.7	$0.46^{+0.08}_{-0.11}$	⋯	39.99	1
J144804.16+182537.8	222.01737	18.42718	0.0378	15.1	10.6	$0.02^{+0.11}_{-0.02}$	7.1	40.00	1
J144804.23+182558.0	222.01764	18.43277	0.0390	15.1	9.6	$0.01^{+0.01}_{-0.00}$	⋯	40.02	0
J151031.75+060007.0	227.63229	6.00195	0.0800	15.2	⋯	⋯	⋯	41.67	0
J151031.66+055957.0	227.63192	5.99919	0.0801	15.2	10.4	$0.01^{+0.05}_{-0.01}$	7.4	41.66	0
J141115.91+573609.0	212.81623	57.60258	0.1062	15.2	11.5	$0.03^{+0.22}_{-0.03}$	8.6	41.37	1
J141115.95+573601.2	212.81638	57.60041	0.1049	15.2	10.7	$0.02^{+0.11}_{-0.02}$	8.4	41.36	0
J111627.21+570659.1	169.11338	57.11651	0.0469	15.2	⋯	⋯	⋯	40.98	0
J111625.68+570709.8	169.10697	57.11950	0.0464	15.2	9.3	$0.24^{+0.01}_{-0.04}$	⋯	41.00	0
J115532.11+583532.5	178.88379	58.59246	0.1644	15.4	11.1	$0.10^{+0.50}_{-0.09}$	8.1	42.72	0
J115532.10+583538.0	178.88375	58.59397	0.1634	15.4	11.1	$0.06^{+0.37}_{-0.06}$	8.2	42.55	0
J142553.53+340452.6	216.47307	34.08129	0.0726	15.4	⋯	⋯	⋯	40.69	0
J142553.20+340442.2	216.47172	34.07840	0.0733	15.4	10.5	$0.01^{+0.07}_{-0.01}$	7.1	40.76	0
J125917.25−013427.8	194.82191	−1.57440	0.1682	15.5	⋯	⋯	⋯	42.39	0
J125917.14−013422.6	194.82143	−1.57297	0.1679	15.5	10.9	$14.68^{+19.47}_{-8.08}$	7.0	42.50	0
J120429.88+022654.6	181.12451	2.44849	0.0200	15.6	9.1	$0.00^{+0.00}_{-0.00}$	⋯	40.09	0
J120432.18+022711.1	181.13413	2.45310	0.0200	15.6	9.6	$0.00^{+0.00}_{-0.00}$	⋯	39.98	0
J125922.72+312213.7	194.84467	31.37050	0.0526	15.8	9.7	$0.04^{+0.03}_{-0.02}$	⋯	40.63	0
J125922.03+312201.1	194.84180	31.36698	0.0524	15.8	9.9	$0.04^{+0.04}_{-0.02}$	⋯	40.63	0
J133525.37+380533.9	203.85570	38.09276	0.0655	16.1	⋯	⋯	⋯	40.97	1
J133525.26+380538.6	203.85305	38.09515	0.0649	16.1	10.0	$0.01^{+0.04}_{-0.01}$	5.7	40.96	0
J142442.81−015929.8	216.17840	−1.99163	0.1746	16.8	11.8	$0.07^{+0.49}_{-0.07}$	8.3	42.72	0
J142442.91−015924.3	216.17881	−1.99011	0.1742	16.8	11.2	$5.82^{+8.22}_{-3.31}$	7.9	42.88	0
J143541.79+330820.0	218.92417	33.13891	0.1206	16.9	⋯	⋯	⋯	42.01	1
J143542.38+330822.1	218.92666	33.13947	0.1205	16.9	11.2	$0.03^{+0.16}_{-0.02}$	7.3	42.01	0
J085405.94+011111.4	133.52477	1.18650	0.0447	17.0	9.4	$0.32^{+0.03}_{-0.06}$	⋯	40.38	0
J085405.90+011130.6	133.52459	1.19186	0.0441	17.0	10.2	$0.43^{+0.06}_{-0.06}$	6.0	40.37	0
J102108.45+482855.4	155.28523	48.48206	0.0618	17.1	10.5	$0.13^{+0.17}_{-0.07}$	7.8	40.78	0
J102109.88+482857.2	155.29119	48.48256	0.0615	17.1	10.1	$0.18^{+0.47}_{-0.14}$	⋯	40.78	1
J111519.23+542310.9	168.83012	54.38636	0.0713	17.1	10.5	$0.01^{+0.04}_{-0.01}$	7.6	40.57	0
J111519.98+542316.7	168.83325	54.38797	0.0704	17.1	11.1	$1.72^{+5.20}_{-1.60}$	8.0	40.62	1
J112402.95+430901.0	171.01229	43.15028	0.0715	17.3	⋯	⋯	⋯	40.36	1
J112401.84+430857.2	171.00768	43.14922	0.0709	17.3	10.5	$1.07^{+0.63}_{-0.38}$	6.9	40.33	1
J171255.40+640145.3	258.23079	64.02934	0.0811	17.5	10.5	$0.01^{+0.08}_{-0.01}$	6.7	40.63	0
J171255.44+640156.7	258.23090	64.03252	0.0813	17.5	10.1	$0.10^{+0.10}_{-0.04}$	⋯	40.60	0
J090215.15+520754.7	135.56311	52.13189	0.1029	17.7	⋯	⋯	⋯	40.95	0
J090215.79+520802.0	135.56578	52.13393	0.1023	17.7	10.2	$1.06^{+0.31}_{-0.14}$	⋯	40.99	1
J110418.11+594831.6	166.07545	59.80882	0.1148	17.8	⋯	⋯	⋯	41.38	0
J110419.26+594830.7	166.08019	59.80861	0.1132	17.8	10.3	$0.43^{+0.53}_{-0.21}$	5.6	41.42	0
J143454.22+334934.5	218.72592	33.82625	0.0578	18.0	10.8	$0.01^{+0.07}_{-0.01}$	7.3	41.06	0
J143454.68+334920.0	218.72783	33.82222	0.0587	18.0	10.7	$0.64^{+1.82}_{-0.58}$	6.7	41.06	0

Table 1
(Continued)

Name (1)	R.A. (2)	Decl. (3)	z (4)	r_p (5)	log M_* (6)	SFR (7)	log M_{BH} (8)	log $L_{X,lim}$ (9)	Flag (10)
J155207.85+273514.6	238.03275	27.58740	0.0747	18.4	⋯	⋯	⋯	40.20	1
J155207.87+273501.6	238.03282	27.58380	0.0748	18.4	11.2	$0.02^{+0.13}_{-0.02}$	8.4	40.28	1
J083902.97+470756.3	129.76239	47.13233	0.0524	18.6	10.7	$0.03^{+0.13}_{-0.02}$	7.3	40.62	1
J083902.50+470814.0	129.76046	47.13722	0.0534	18.6	10.5	$1.21^{+0.30}_{-0.17}$	7.6	40.64	0
J214622.41+000452.1	326.59337	0.08114	0.0754	18.7	10.4	$4.72^{+10.33}_{-3.39}$	6.1	41.22	0
J214623.23+000456.7	326.59679	0.08242	0.0750	18.7	10.9	$2.72^{+6.49}_{-2.04}$	7.2	41.22	1
J123042.83+103445.3	187.67848	10.57926	0.1636	19.6	⋯	⋯	⋯	41.88	0
J123043.27+103442.9	187.68033	10.57860	0.1636	19.6	11.5	$0.06^{+0.38}_{-0.06}$	8.7	41.86	0
J161111.72+522645.6	242.79888	52.44607	0.0605	19.7	⋯	⋯	⋯	40.90	0
J161113.52+522649.3	242.80639	52.44709	0.0607	19.7	10.3	$0.92^{+0.81}_{-0.41}$	⋯	40.86	1

Note. (1) SDSS names with J2000 coordinates given in the form of "hhmmss.ss+ddmmss.s;" (2)–(3) optical position of the galaxy nucleus; (4) redshift; (5) projected physical separation of galaxies in each pair, in units of kpc; (6) stellar mass, in units of $M_\odot$; (7) star formation rate, in units of $M_\odot$ yr^{-1}, given by the MPA-JHU DR7 catalog; (8) black hole mass estimate inferred from σ_* assuming the M_{BH}–σ_* relation of Gültekin et al. (2009), in units of $M_\odot$; (9) 0.5–8 keV limiting luminosity for source detection, in units of erg s^{-1}; (10) flag for X-ray detection, 1 and 0 represent detection and non-detection in X-ray, respectively.

(This table is available in machine-readable form.)

PSF maps supplied and a false detection probability of 10^{-6}. We then searched for an X-ray counterpart of each optical nucleus from the X-ray source lists output by *wavdetect*, adopting a matching radius of 2″, an empirically optimal value given the angular resolution and astrometry accuracy of Chandra in most cases. This is further justified by a random matching test by artificially shifting the positions of all nuclei by ±10″ in R.A. and decl., which finds on average less than one coincident match with the detected X-ray sources. We note that no pair in our sample has angular separation less than this matching radius (see the third panel in Figure 1), which means two nuclei in a pair would not be matched with one identical X-ray counterpart in any case. If the optical nucleus was matched with an X-ray counterpart in any of the three energy bands, we consider it to be X-ray detected.

Source photometry was then calculated using the CIAO tool *aprate*, which properly handles the counting statistics in the low-count regime. Source count at a given band was extracted from within the 90% enclosed count radius (ECR). The local background was evaluated from a concentric annulus with inner-to-outer radii 2–5 times the 90% ECR for the inner radius, excluding pixels falling within the 90% ECR of neighboring sources, if any. In a few cases where the two nuclei have overlapping 90% ECR, we adopt the 50% ECR for photometry. The net photon flux was derived by dividing the exposure map and corrected for the ECF.

For the optical nuclei without an X-ray counterpart found by *wavdetect*, we extracted the source and background counts in a similar way and estimated a 3σ upper limit of the net photon flux using *aprate*. If the 3σ lower limit were greater than zero, the nucleus is regarded as an X-ray detection. Using this more quantitative criterion, we recover a few more nuclei with significant X-ray emission that have been filtered by *wavdetect*. For the remaining nuclei, we again used *aprate* to derive a 3σ upper limit of the net photon flux.

The net photon fluxes (or upper limits) were then converted to an unabsorbed luminosity in the 0.5–2 and 2–10 keV bands, by multiplying a unique conversion factor for a given energy band according to the fiducial incident spectrum described in Section 3.1. The net counts, photon fluxes, and luminosities are listed in Table 2. We have also determined the detection limit of a given band at the position of each nucleus, following the method of Kashyap et al. (2010). Figure 2 plots the histogram of the 0.5–8 limiting luminosity for both the current sample (listed in Table 1) and the AGN pairs of Hou et al. (2020), which have a similar distribution, facilitating a direct comparison between the two sample.

3.3. NuSTAR Spectral Analysis

To help constrain the presence of intrinsically luminous but heavily obscured AGNs in the sample galaxies, we utilized archival NuSTAR observations that are sensitive to the hard ($\gtrsim$10 keV) X-rays from obscured AGNs. Eight pairs in the current sample have been observed by NuSTAR, with an effective exposure ranging from 19.5 to 211.3 ks. We note that half of these eight observations were taken as a targeted observation to probe the hard X-ray emission from a putative AGN.

The NuSTAR data were downloaded and reprocessed following the standard *nupipeline* in the software package NuSTARDAS v2.1.2. The spectra of each galaxy pair were extracted for both focal plane modules A and B (FPMA and FPMB) with *nuproducts*. A circular region was used to extract the source spectrum, which has a radius of 60″, approximately equaling 75% ECR. Since the two nuclei in a given pair are not well resolved by NuSTAR, the source center was set to be the brighter nucleus as seen by Chandra, which is generally consistent with the peak of the NuSTAR-detected signal. The background spectra were extracted from a concentric annulus with an inner radius of 90″ and an outer radius of 150″. It turns out that three of the eight pairs show no significant signal above the background, thus they were neglected in the spectral analysis.

For the five pairs with significant hard X-ray emission, the spectra were grouped to achieve a signal-to-noise ratio (S/N) greater than 3 per bin over the energy range of 3–79 keV. We follow the method of Zappacosta et al. (2018) to simulate background spectrum using the software NUSKYBGD (Wik et al. 2014) to account for the spatially dependent background of NuSTAR. This task aims to compute the relative strengths of different background components and hence well reproduce the

Table 2
X-Ray Properties of Close Galaxy Pairs

Name (1)	XR.A. (2)	XDecl. (3)	Counts (4)	$F_{0.5-2}$ (5)	F_{2-8} (6)	log $L_{0.5-2}$ (7)	log L_{2-10} (8)	HR (9)
J102700.56+174900.3	156.75230	17.81692	$55.1^{+8.3}_{-8.2}$	$2.30^{+0.42}_{-0.38}$	$0.79^{+0.26}_{-0.22}$	$40.73^{+0.07}_{-0.08}$	$40.85^{+0.13}_{-0.14}$	$-0.76^{+0.02}_{-0.24}$
J085837.53+182221.6	134.65689	18.37266	$18.7^{+4.9}_{-4.3}$	$2.55^{+0.67}_{-0.58}$	<0.19	$40.66^{+0.10}_{-0.11}$	<40.13	$-0.95^{+0.00}_{-0.05}$
J085837.68+182223.4	134.65689	18.37266	$14.2^{+4.4}_{-3.7}$	$1.79^{+0.57}_{-0.48}$	$0.15^{+0.25}_{-0.13}$	$40.51^{+0.12}_{-0.14}$	$40.04^{+0.42}_{-0.75}$	$-0.83^{+0.04}_{-0.17}$
J105842.44+314457.6	164.67683	31.74933	$2.6^{+2.3}_{-1.6}$	$0.30^{+0.35}_{-0.23}$	<0.46	$39.92^{+0.34}_{-0.65}$	<40.70	$-0.26^{+0.26}_{-0.74}$
J105842.58+314459.8	164.67744	31.74995	$96.1^{+10.4}_{-10.3}$	$1.36^{+0.60}_{-0.48}$	$18.40^{+2.00}_{-2.10}$	$40.57^{+0.16}_{-0.19}$	$42.30^{+0.04}_{-0.05}$	$0.82^{+0.08}_{-0.05}$
J002208.69+002200.5	5.53621	0.36681	$11.9^{+6.0}_{-4.8}$	$0.58^{+0.29}_{-0.23}$	<0.13	$40.19^{+0.18}_{-0.22}$	<40.12	$-0.87^{+0.01}_{-0.13}$
J002208.83+002202.8	5.53679	0.36744	$7.8^{+5.2}_{-4.0}$	$0.28^{+0.22}_{-0.16}$	$0.14^{+0.19}_{-0.13}$	$39.87^{+0.26}_{-0.37}$	$40.17^{+0.37}_{-0.88}$	$-0.41^{+0.17}_{-0.59}$
J133032.00−003613.5	202.63333	−0.60379	$17.3^{+4.8}_{-4.1}$	$2.31^{+0.75}_{-0.63}$	$1.12^{+0.57}_{-0.45}$	$40.54^{+0.12}_{-0.14}$	$40.82^{+0.18}_{-0.23}$	$-0.42^{+0.16}_{-0.25}$
J141447.15−000013.3	213.69646	−0.00376	$1188.2^{+36.4}_{-36.0}$	$27.60^{+1.50}_{-1.50}$	$40.40^{+1.50}_{-1.50}$	$41.50^{+0.02}_{-0.02}$	$42.26^{+0.02}_{-0.02}$	$0.04^{+0.03}_{-0.04}$
J141447.48−000011.3	213.69783	−0.00321	$556.3^{+25.0}_{-24.7}$	$21.70^{+1.40}_{-1.30}$	$11.90^{+0.80}_{-0.90}$	$41.40^{+0.03}_{-0.03}$	$41.73^{+0.03}_{-0.03}$	$-0.42^{+0.04}_{-0.04}$
J235654.30−101605.4	359.22646	−10.26818	$526.7^{+24.2}_{-24.0}$	$24.30^{+3.40}_{-3.40}$	$188.03^{+9.16}_{-9.06}$	$41.85^{+0.06}_{-0.07}$	$43.33^{+0.02}_{-0.02}$	$0.74^{+0.03}_{-0.03}$
J122814.15+442711.7	187.05896	44.45325	$14.3^{+6.3}_{-5.2}$	$17.80^{+21.20}_{-13.85}$	$73.90^{+36.53}_{-28.40}$	$40.68^{+0.34}_{-0.65}$	$41.89^{+0.17}_{-0.21}$	$0.57^{+0.43}_{-0.11}$
J122815.23+442711.3	187.06348	44.45314	$12.1^{+6.0}_{-4.8}$	$71.60^{+34.93}_{-27.40}$	<25.80	$41.27^{+0.17}_{-0.21}$	<41.42	$-0.42^{+0.18}_{-0.58}$
J112648.50+351503.2	171.70213	35.25081	$5273.1^{+76.6}_{-75.9}$	$469.87^{+9.51}_{-9.41}$	$500.68^{+10.47}_{-10.37}$	$42.39^{+0.01}_{-0.01}$	$43.01^{+0.01}_{-0.01}$	$-0.13^{+0.01}_{-0.01}$
J112648.65+351454.2	171.70263	35.24838	$9.5^{+3.9}_{-3.2}$	$1.54^{+0.64}_{-0.53}$	<0.43	$39.90^{+0.15}_{-0.18}$	<39.94	$-0.83^{+0.03}_{-0.17}$
J090025.37+390353.7	135.10567	39.06513	$7.8^{+2.9}_{-2.8}$	$0.35^{+0.30}_{-0.21}$	$1.16^{+0.59}_{-0.47}$	$39.79^{+0.26}_{-0.40}$	$40.90^{+0.18}_{-0.22}$	$0.37^{+0.41}_{-0.21}$
J151806.13+424445.0	229.52559	42.74580	$76.4^{+9.4}_{-9.3}$	$10.20^{+1.30}_{-1.35}$	$2.44^{+0.83}_{-0.69}$	$40.92^{+0.05}_{-0.06}$	$40.90^{+0.13}_{-0.14}$	$-0.68^{+0.07}_{-0.10}$
J151806.37+424438.1	229.52648	42.74393	$15.1^{+4.5}_{-3.9}$	$2.36^{+0.70}_{-0.61}$	<0.26	$40.30^{+0.11}_{-0.13}$	<39.93	$-0.93^{+0.00}_{-0.07}$
J104518.04+351913.1	161.32538	35.32022	$28.2^{+6.1}_{-5.5}$	$1.84^{+0.48}_{-0.42}$	$0.58^{+0.25}_{-0.20}$	$40.64^{+0.10}_{-0.11}$	$40.74^{+0.16}_{-0.19}$	$-0.60^{+0.11}_{-0.16}$
J104518.43+351913.5	161.32676	35.32023	$10.6^{+4.2}_{-3.5}$	$0.55^{+0.31}_{-0.24}$	$0.52^{+0.24}_{-0.19}$	$40.11^{+0.19}_{-0.26}$	$40.69^{+0.16}_{-0.20}$	$-0.11^{+0.25}_{-0.38}$
J133817.27+481632.3	204.57207	48.27566	$92.6^{+10.6}_{-10.5}$	$16.30^{+2.10}_{-2.00}$	$4.94^{+1.47}_{-1.25}$	$40.80^{+0.05}_{-0.06}$	$40.87^{+0.11}_{-0.13}$	$-0.61^{+0.07}_{-0.11}$
J133817.77+481641.1	204.57415	48.27808	$209.4^{+15.5}_{-15.3}$	$26.00^{+2.60}_{-2.50}$	$27.40^{+3.10}_{-3.10}$	$41.00^{+0.04}_{-0.04}$	$41.61^{+0.05}_{-0.05}$	$-0.17^{+0.06}_{-0.08}$
J114753.63+094552.0	176.97337	9.76444	$3302.0^{+60.7}_{-60.1}$	$112.86^{+4.55}_{-4.51}$	$361.19^{+7.45}_{-7.38}$	$42.74^{+0.02}_{-0.02}$	$43.84^{+0.01}_{-0.01}$	$0.44^{+0.02}_{-0.02}$
J093634.03+232627.0	144.14171	23.44080	$7.6^{+3.3}_{-2.7}$	$5.22^{+2.39}_{-1.93}$	$0.79^{+1.26}_{-0.67}$	$40.32^{+0.16}_{-0.20}$	$40.10^{+0.41}_{-0.81}$	$-0.75^{+0.05}_{-0.25}$
J084113.09+322459.6	130.30458	32.41649	$187.9^{+14.6}_{-14.5}$	$4.00^{+0.36}_{-0.35}$	$1.84^{+0.28}_{-0.27}$	$40.99^{+0.04}_{-0.04}$	$41.25^{+0.06}_{-0.07}$	$-0.48^{+0.06}_{-0.07}$
J140737.43+442855.1	211.90597	44.48199	$1064.1^{+34.5}_{-34.1}$	$38.30^{+2.40}_{-2.30}$	$79.30^{+3.00}_{-3.00}$	$42.65^{+0.03}_{-0.03}$	$43.56^{+0.02}_{-0.02}$	$0.21^{+0.03}_{-0.03}$
J084135.08+010156.1	130.39612	1.03229	$366.7^{+20.3}_{-20.1}$	$12.60^{+1.00}_{-1.00}$	$14.30^{+1.10}_{-1.00}$	$41.93^{+0.03}_{-0.04}$	$42.58^{+0.03}_{-0.03}$	$-0.08^{+0.06}_{-0.05}$
J230010.17−000531.5	345.04272	−0.09205	$14.7^{+4.7}_{-4.0}$	$1.10^{+0.43}_{-0.35}$	$0.19^{+0.18}_{-0.12}$	$41.32^{+0.14}_{-0.17}$	$41.16^{+0.28}_{-0.40}$	$-0.73^{+0.08}_{-0.21}$
J112536.15+542257.2	171.40069	54.38269	$3830.9^{+65.3}_{-64.7}$	$785.97^{+17.37}_{-17.19}$	$635.29^{+17.06}_{-16.89}$	$42.22^{+0.01}_{-0.01}$	$42.72^{+0.01}_{-0.01}$	$-0.19^{+0.02}_{-0.02}$
J083817.59+305453.5	129.57323	30.91485	$7.8^{+2.9}_{-2.8}$	$5.26^{+2.17}_{-2.04}$	$0.77^{+1.05}_{-0.60}$	$40.79^{+0.15}_{-0.21}$	$40.55^{+0.37}_{-0.66}$	$-0.73^{+0.06}_{-0.26}$
J110713.23+650606.6	166.80544	65.10198	$4.3^{+2.6}_{-2.0}$	$1.69^{+1.59}_{-1.05}$	$1.50^{+1.38}_{-0.90}$	$39.96^{+0.29}_{-0.42}$	$40.50^{+0.28}_{-0.40}$	$-0.15^{+0.33}_{-0.58}$
J110713.49+650553.2	166.80633	65.09846	$3.3^{+2.3}_{-1.7}$	$2.61^{+1.84}_{-1.32}$	$0.77^{+1.05}_{-0.60}$	$40.13^{+0.23}_{-0.31}$	$40.19^{+0.37}_{-0.66}$	$-0.53^{+0.11}_{-0.47}$
J090714.45+520343.4	136.81026	52.06206	$40.7^{+7.1}_{-6.4}$	$1.01^{+0.54}_{-0.40}$	$7.36^{+1.39}_{-1.24}$	$40.27^{+0.19}_{-0.22}$	$41.73^{+0.08}_{-0.08}$	$0.69^{+0.15}_{-0.09}$
J090714.61+520350.7	136.81087	52.06413	$120.9^{+11.6}_{-11.5}$	$4.93^{+1.05}_{-0.97}$	$19.60^{+2.10}_{-2.10}$	$40.97^{+0.08}_{-0.10}$	$42.16^{+0.04}_{-0.05}$	$0.52^{+0.09}_{-0.07}$
J134736.41+173404.7	206.90178	17.56801	$67.8^{+8.7}_{-8.6}$	$86.40^{+11.50}_{-11.50}$	$9.84^{+4.56}_{-4.12}$	$41.95^{+0.05}_{-0.06}$	$41.59^{+0.17}_{-0.24}$	$-0.82^{+0.04}_{-0.09}$
J000249.07+004504.8	0.70433	0.75128	$18.1^{+5.2}_{-6.3}$	$5.54^{+2.76}_{-2.61}$	$7.21^{+3.09}_{-3.11}$	$41.35^{+0.18}_{-0.28}$	$42.06^{+0.15}_{-0.25}$	$-0.08^{+0.28}_{-0.34}$
J094543.54+094901.5	146.43146	9.81709	$13.5^{+6.4}_{-5.2}$	$0.74^{+0.78}_{-0.50}$	$1.27^{+0.71}_{-0.56}$	$41.02^{+0.31}_{-0.49}$	$41.84^{+0.19}_{-0.25}$	$0.10^{+0.49}_{-0.43}$
J085953.33+131055.3	134.97212	13.18192	$477.5^{+23.1}_{-22.8}$	$0.88^{+0.55}_{-0.41}$	$89.20^{+4.40}_{-4.30}$	$39.63^{+0.21}_{-0.27}$	$42.22^{+0.02}_{-0.02}$	$0.97^{+0.02}_{-0.01}$
J123515.49+122909.0	188.81481	12.48569	$31.4^{+9.7}_{-8.4}$	$0.82^{+0.33}_{-0.28}$	$0.64^{+0.30}_{-0.24}$	$40.00^{+0.15}_{-0.18}$	$40.48^{+0.17}_{-0.21}$	$-0.25^{+0.24}_{-0.27}$
J161758.52+345439.9	244.49387	34.91109	$3.0^{+3.5}_{-2.3}$	$1.39^{+1.43}_{-0.92}$	<0.95	$41.25^{+0.31}_{-0.47}$	<41.68	$-0.64^{+0.04}_{-0.36}$
J095749.15+050638.3	149.45481	5.11066	$9.4^{+5.2}_{-4.0}$	$0.45^{+0.71}_{-0.38}$	$1.08^{+0.68}_{-0.50}$	$40.57^{+0.41}_{-0.84}$	$41.54^{+0.21}_{-0.27}$	$0.21^{+0.79}_{-0.26}$
J123637.50+163344.6	189.15634	16.56247	$163.2^{+13.8}_{-13.7}$	$15.00^{+1.30}_{-1.30}$	$0.96^{+0.37}_{-0.30}$	$41.63^{+0.04}_{-0.04}$	$41.03^{+0.14}_{-0.16}$	$-0.90^{+0.02}_{-0.04}$
J124545.20+010447.5	191.43838	1.08009	$6.6^{+3.1}_{-2.5}$	$2.13^{+0.98}_{-0.79}$	<0.59	$41.12^{+0.16}_{-0.20}$	<41.16	$-0.85^{+0.01}_{-0.15}$
J090134.48+180942.9	135.39369	18.16188	$27.3^{+5.9}_{-5.2}$	<1.07	$12.60^{+2.90}_{-2.50}$	<40.39	$42.06^{+0.09}_{-0.10}$	$0.92^{+0.08}_{-0.01}$
J105622.07+421807.8	164.09197	42.30219	$41.1^{+7.4}_{-6.7}$	$0.56^{+0.11}_{-0.11}$	$0.14^{+0.05}_{-0.05}$	$40.25^{+0.08}_{-0.09}$	$40.23^{+0.15}_{-0.18}$	$-0.68^{+0.10}_{-0.12}$
J132924.25+114749.3	202.35106	11.79699	$16.7^{+4.8}_{-4.2}$	$0.90^{+0.28}_{-0.24}$	$0.18^{+0.17}_{-0.11}$	$39.32^{+0.12}_{-0.13}$	$39.22^{+0.29}_{-0.42}$	$-0.70^{+0.10}_{-0.23}$
J135429.06+132757.3	208.62108	13.46604	$234.2^{+16.2}_{-16.0}$	$2.80^{+1.13}_{-0.92}$	$75.10^{+5.30}_{-5.20}$	$40.77^{+0.15}_{-0.17}$	$42.79^{+0.03}_{-0.03}$	$0.91^{+0.04}_{-0.02}$
J125725.84+273246.0	194.35769	27.54613	$21.4^{+7.1}_{-6.4}$	$0.52^{+0.25}_{-0.22}$	$0.33^{+0.16}_{-0.14}$	$38.95^{+0.17}_{-0.23}$	$39.35^{+0.17}_{-0.24}$	$-0.33^{+0.26}_{-0.34}$
J011448.67−002946.0	18.70286	−0.49634	$1097.0^{+35.0}_{-34.6}$	$163.66^{+6.64}_{-6.57}$	$86.20^{+4.50}_{-4.40}$	$41.98^{+0.02}_{-0.02}$	$42.29^{+0.02}_{-0.02}$	$-0.40^{+0.03}_{-0.03}$
J145051.50+050652.1	222.71453	5.11454	$208.4^{+15.3}_{-15.1}$	$38.20^{+3.10}_{-3.10}$	$9.17^{+1.33}_{-1.53}$	$41.16^{+0.03}_{-0.04}$	$41.13^{+0.06}_{-0.08}$	$-0.68^{+0.05}_{-0.05}$
J145050.63+050710.8	222.71082	5.11957	$32.9^{+6.4}_{-5.8}$	$3.81^{+1.08}_{-0.93}$	$3.41^{+0.96}_{-0.83}$	$40.18^{+0.11}_{-0.12}$	$40.73^{+0.11}_{-0.12}$	$-0.17^{+0.18}_{-0.17}$
J134844.49+271044.7	207.18541	27.17911	$10.9^{+4.6}_{-3.9}$	$0.31^{+0.17}_{-0.13}$	$0.18^{+0.12}_{-0.10}$	$39.77^{+0.19}_{-0.24}$	$40.12^{+0.23}_{-0.34}$	$-0.40^{+0.30}_{-0.38}$
J090005.15+391952.2	135.02133	39.33119	$8.5^{+3.5}_{-2.9}$	$4.97^{+2.00}_{-1.64}$	<0.88	$41.39^{+0.15}_{-0.17}$	<41.23	$-0.89^{+0.01}_{-0.11}$
J125315.99−031036.4	193.31665	−3.17680	$2.0^{+2.0}_{-1.3}$	$3.00^{+2.51}_{-1.81}$	<0.91	$41.07^{+0.26}_{-0.40}$	<41.14	$-0.84^{+-0.01}_{-0.16}$
J125359.62+462750.2	193.49847	46.46392	$15.6^{+3.8}_{-4.3}$	$19.20^{+4.90}_{-5.40}$	$1.83^{+2.52}_{-1.43}$	$41.58^{+0.10}_{-0.14}$	$41.15^{+0.38}_{-0.66}$	$-0.81^{+0.04}_{-0.19}$
J080133.94+141334.0	120.38814	14.22832	$7.4^{+3.3}_{-2.7}$	$0.44^{+0.21}_{-0.17}$	$0.14^{+0.14}_{-0.09}$	$39.80^{+0.17}_{-0.21}$	$39.89^{+0.31}_{-0.47}$	$-0.59^{+0.10}_{-0.41}$
J144804.16+182537.8	222.01737	18.42721	$14.0^{+4.4}_{-3.7}$	$1.16^{+0.47}_{-0.38}$	$0.48^{+0.36}_{-0.26}$	$39.93^{+0.15}_{-0.18}$	$40.13^{+0.24}_{-0.33}$	$-0.50^{+0.19}_{-0.29}$

Table 2
(Continued)

Name (1)	XR.A. (2)	XDecl. (3)	Counts (4)	$F_{0.5-2}$ (5)	F_{2-8} (6)	log $L_{0.5-2}$ (7)	log L_{2-10} (8)	HR (9)
J141115.91+573609.0	212.81623	57.60258	$20.2^{+5.4}_{-4.8}$	$1.83^{+1.03}_{-0.80}$	<0.76	$41.05^{+0.19}_{-0.25}$	<41.27	$-0.77^{+0.03}_{-0.23}$
J133525.37+380533.9	203.85554	38.09311	$62.8^{+11.4}_{-11.2}$	$9.54^{+2.16}_{-1.90}$	$4.73^{+1.55}_{-1.31}$	$41.33^{+0.09}_{-0.10}$	$41.62^{+0.12}_{-0.14}$	$-0.42^{+0.12}_{-0.17}$
J143541.79+330820.0	218.92417	33.13891	$5.8^{+4.2}_{-3.0}$	$3.15^{+2.98}_{-1.93}$	$1.61^{+2.09}_{-1.27}$	$41.41^{+0.29}_{-0.41}$	$41.71^{+0.36}_{-0.68}$	$-0.36^{+0.22}_{-0.59}$
J102109.88+482857.2	155.29119	48.48256	$5.2^{+2.9}_{-2.2}$	$0.81^{+0.59}_{-0.41}$	$0.28^{+0.51}_{-0.27}$	$40.20^{+0.24}_{-0.31}$	$40.33^{+0.45}_{-1.58}$	$-0.50^{+0.14}_{-0.50}$
J111519.98+542316.7	168.83312	54.38789	$1498.0^{+40.9}_{-40.5}$	$17.30^{+1.70}_{-1.60}$	$218.16^{+6.22}_{-6.16}$	$41.65^{+0.04}_{-0.04}$	$43.35^{+0.01}_{-0.01}$	$0.82^{+0.02}_{-0.02}$
J112402.95+430901.0	171.01226	43.15025	$29.2^{+7.1}_{-6.5}$	$0.97^{+0.27}_{-0.24}$	$0.22^{+0.13}_{-0.12}$	$40.42^{+0.11}_{-0.12}$	$40.37^{+0.21}_{-0.32}$	$-0.72^{+0.16}_{-0.18}$
J112401.84+430857.2	171.00768	43.14922	$12.0^{+5.2}_{-4.6}$	$0.35^{+0.17}_{-0.14}$	$0.12^{+0.11}_{-0.09}$	$39.97^{+0.17}_{-0.22}$	$40.09^{+0.28}_{-0.60}$	$-0.61^{+0.11}_{-0.39}$
J090215.79+520802.0	135.56578	52.13393	$5.8^{+3.1}_{-2.4}$	$0.32^{+0.23}_{-0.16}$	$0.24^{+0.22}_{-0.15}$	$40.26^{+0.24}_{-0.31}$	$40.73^{+0.28}_{-0.45}$	$-0.30^{+0.37}_{-0.49}$
J155207.85+273514.6	238.03275	27.58741	$9.1^{+4.4}_{-3.7}$	$0.26^{+0.15}_{-0.12}$	$0.10^{+0.09}_{-0.06}$	$39.88^{+0.20}_{-0.29}$	$40.04^{+0.29}_{-0.49}$	$-0.48^{+0.10}_{-0.52}$
J155207.87+273501.6	238.03274	27.58389	$234.2^{+16.3}_{-16.1}$	$7.68^{+0.64}_{-0.62}$	$3.14^{+0.40}_{-0.40}$	$41.36^{+0.03}_{-0.04}$	$41.56^{+0.05}_{-0.06}$	$-0.52^{+0.05}_{-0.06}$
J083902.97+470756.3	129.76228	47.13214	$70.6^{+8.9}_{-8.8}$	$1.58^{+0.86}_{-0.67}$	$20.00^{+2.60}_{-2.60}$	$40.35^{+0.19}_{-0.24}$	$42.04^{+0.05}_{-0.06}$	$0.78^{+0.11}_{-0.07}$
J214623.23+000456.7	326.59679	0.08242	$6.3^{+3.3}_{-2.7}$	<0.49	$1.93^{+0.94}_{-0.76}$	<40.16	$41.35^{+0.17}_{-0.22}$	$0.78^{+0.22}_{-0.03}$
J161113.52+522649.3	242.80594	52.44716	$10.4^{+3.9}_{-3.2}$	$1.54^{+0.75}_{-0.59}$	$0.98^{+0.64}_{-0.48}$	$40.47^{+0.17}_{-0.21}$	$40.87^{+0.22}_{-0.29}$	$-0.32^{+0.21}_{-0.39}$

Note. (1) SDSS names with J2000 coordinates given in the form of "hhmmss.ss+ddmmss.s;" (2)–(3) centroid position of the X-ray counterpart; (4) observed net counts in 0.5–8 (F) keV bands; (5)–(6) observed photon flux in 0.5–2 (S) and 2–8 (H) keV bands, in units of 10^{-6} ph cm^{-2} s^{-1}; (7)–(8) 0.5–2 and 2–10 keV unabsorbed luminosities, in units of erg s^{-1}; (9) hardness ratio between the 0.5–2 and 2–8 keV bands.

(This table is available in machine-readable form.)

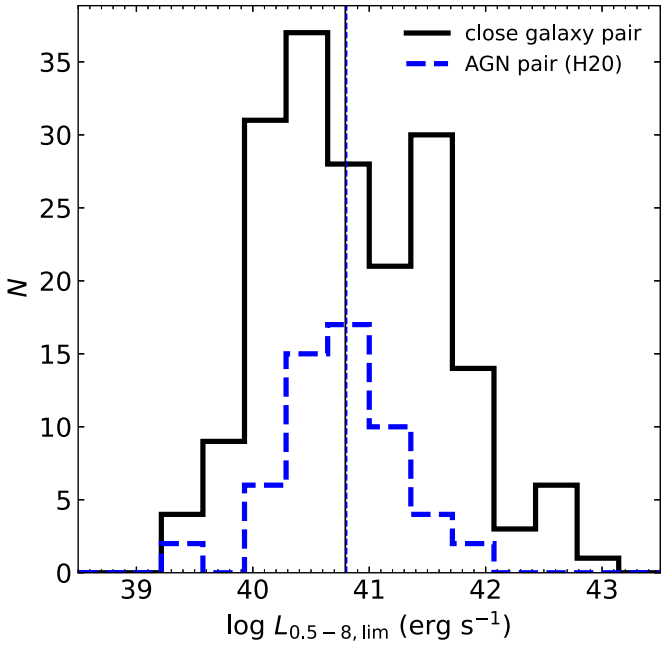

Figure 2. 0.5–8 keV detection limit distribution of the close galaxy pairs studied in this work (black solid histogram), in comparison with the close AGN pairs (blue dashed) in Hou et al. (2020). The vertical lines mark the median value of the individual samples.

background spectrum at each position of the detector. The FPMA/FPMB spectra were jointly fitted. Spectral analysis was carried out with Xspec v.12.12.1c, adopting the χ^2 statistics to determine the best-fit model. Since we are mainly interested in constraining the line-of-sight absorption column density and the intrinsic X-ray luminosity, we adopted a phenomenological model, an absorbed power law model *tbabs*∗*powerlaw*, as the default model. In one source, J1451+0507, significant excess is present around 6.4 keV, which can be interpreted as an iron fluorescent emission line often seen in luminous AGNs. For this source, we added a Gaussian component to account for the putative Fe line, which significantly improved the fit. Such a Gaussian component was not required for the other four sources. The spectral fit results are listed in Table 3, which include the best-fit absorption column density, photon index, 3–79 keV unabsorbed flux and 2–10 keV unabsorbed luminosity converted from the best-fit model.

4. Results

4.1. X-Ray Detection Rate

A bright X-ray source matched with the galactic nucleus usually refers to an AGN, but with potential contamination from the host galaxy (i.e., nuclear starburst). As estimated in Section 4.2, The X-ray emission due to star formation is neglectable compared to AGN, especially for the nuclei with $L_{2-10} > 10^{41}$ erg s^{-1}.

In total, we find 70 X-ray-detected nuclei, among which 67 are detected in the S band, 58 are detected in the H band, and 70 are detected in the F band. Among the 92 close galaxy pairs, 14 pairs have both nuclei detected, 42 pairs have only one of the two nuclei detected, and 36 pairs have no X-ray detection. Figure 3 displays the SDSS *gri* color-composite images and the Chandra 0.5–8 keV images of the newly-found close galaxy pairs with both nuclei detected in the X-rays (the other six pairs have been studied and presented in Hou et al. 2020). These 16 nuclei have a 0.5–8 keV luminosity ranging from 1.3×10^{40}–6.3×10^{42} erg s^{-1}.

We find an X-ray detection rate of $38\%^{+5\%}_{-5\%}$ (70/184) among the 92 close galaxy pairs. The quoted error takes into account the counting (Poisson) error in both the numerator and denominator. In the more conservative case, where we only consider X-ray counterparts with a 2–10 keV unabsorbed luminosity $L_{2-10} > 10^{41}$ erg s^{-1}, which are most likely dominated by an AGN (see Section 4.2), the detection rate becomes $18\%^{+3\%}_{-3\%}$ (32/184). For comparison, Hou et al. (2020) gave a detection rate of $27\%^{+5\%}_{-5\%}$ (36/134) for their entire sample of AGNs (i.e., regardless of the value of r_p) above the threshold of $L_{2-10} = 10^{41}$ erg s^{-1}. This factor of ∼1.5 difference may be understood as a systematically higher fraction of true AGNs in

Table 3
NuSTAR Spectral Fit Results

Name (1)	Observation ID (2)	$N_{\rm H}$ (3)	Γ (4)	χ^2/d. o. f (5)	F_{3-79} (6)	$L_{2-10,\rm N}$ (7)	$L_{2-10,\rm C}$ (8)
J0841+0102	60401002002	$0.03^{+7.15}_{-0.03}$	$0.61^{+0.25}_{-0.13}$	37.48/48	$8.82^{+1.78}_{-2.05}$	$43.16^{+0.12}_{-0.05}$	$42.58^{+0.03}_{-0.03}$
J1125+5423	60160430002	$0.78^{+2.50}_{-0.78}$	$1.59^{+0.13}_{-0.09}$	199.88/203	$8.11^{+0.73}_{-0.67}$	$42.34^{+0.06}_{-0.04}$	$42.72^{+0.01}_{-0.01}$
J1338+4816	60465005002	$2.09^{+10.08}_{-2.09}$	$1.3^{+0.41}_{-0.25}$	42.13/38	$3.17^{+1.03}_{-0.77}$	$42.02^{+0.19}_{-0.10}$	$41.61^{+0.05}_{-0.05}$
J1354+1328	60160565002	$17.53^{+4.59}_{-3.99}$	$1.45^{+0.14}_{-0.13}$	166.38/183	$14.81^{+1.32}_{-1.19}$	$43.51^{+0.07}_{-0.07}$	$42.79^{+0.03}_{-0.03}$
J1450+0507	60301025002	$0.02^{+17.78}_{-0.02}$	$-0.27^{+0.40}_{-0.32}$	32.88/35	$13.08^{+6.10}_{-4.59}$	$41.50^{+0.18}_{-0.07}$	$41.13^{+0.06}_{-0.08}$

Note. (1) Source name; (2) NuSTAR observation ID; (3) best-fit column density, in units of 10^{22} cm^{-2}; (4) best-fit photon index; (5) χ^2 over degree of freedom; (6) 3–79 keV unabsorbed flux derived from the best-fit spectral model, in units of 10^{-12} erg s^{-1} cm^{-2}; (7) 2–10 keV intrinsic luminosity derived from the NuSTAR spectrum; (8) 2–10 keV intrinsic luminosity of the brighter nucleus derived from Chandra data.

the Hou et al. (2020) sample, which is consistent with their original optical classification. When considering the fraction of pairs containing at least one X-ray-detected nucleus with $L_{2-10} > 10^{41}$, we find $32\%^{+7\%}_{-7\%}$ (30 out of 92 pairs) for the current sample, which is again somewhat lower than that of the Hou et al. (2020) AGN sample ($47\%^{+11\%}_{-10\%}$; 32 out of 67 pairs). These and additional detection rates are reported in Table 4.

4.2. Global X-Ray Properties

The left panel of Figure 4 shows L_{2-10} against the hardness ratio of the 70 X-ray-detected nuclei in the close galaxy pairs (black squares). The hardness ratio, which is defined as HR $= (H - S)/(H + S)$, is calculated from the observed photon flux in the S (0.5–2 keV) and H (2–8 keV) bands using a Bayesian approach (Park et al. 2006). For the nuclei that are not detected in the H band, we show the 3σ upper limit of L_{2-10} by arrows in the plot. The X-ray counterparts of the AGN pairs (blue circles) and SFG pairs (red triangles) from Hou et al. (2020) are also plotted for comparison (excluding those already included in the new sample).

Sixteen nuclei in the current sample are found to have $L_{2-10} > 10^{42}$ erg s^{-1}. These 16 nuclei are probably bona fide AGNs, but notably only four of them are found in a pair containing another X-ray-detected nucleus (J0907+5203, J1058+3144, J1126+3515, and J1414−0000). The majority of close galaxy pairs, however, are found at the bottom left portion with relatively low luminosities ($L_{2-10} < 10^{41}$ erg s^{-1}) and a negative HR (i.e., a soft spectrum), a region also occupied by most SFG pairs. This may suggest that the X-ray emission of these nuclei are dominated by SF activities (e.g., high-mass X-ray binaries and circumnuclear hot gas heated by supernovae) rather than an AGN. However, this does not totally preclude the possibility that some of these sources host an accreting SMBH, either intrinsically weak or heavily obscured by circumnulcear cold gas with a high column density. In such a case, the observed soft X-rays probably arise further away from the SMBH.

Seventy-five nuclei in the current sample have reliable optical emission-line measurements provided by the MPA-JHU SDSS DR7 catalog.[9] For these nuclei, we plot a standard BPT diagram (Baldwin et al. 1981), utilizing the line ratios of [O III]/Hβ and [N II]/Hα to provide a canonical diagnosis of their nature, namely, SF, AGN, or SF/AGN composite, as shown in the right panel of Figure 4. Forty-eight of the 75 nuclei can be classified as an AGN or composite, the majority of which are X-ray detected. The remaining 27 nuclei are classified as SF nuclei, but only eight (∼30%) of them are X-ray-detected, suggesting that the SF activity does not contribute strongly to the observed X-ray emission, at least in this subset of the sample with optical emission-line measurements. We note that only two pairs in our sample have both nuclei classified as SF.

We further use SDSS spectroscopic star-formation rates (SFRs; Brinchmann et al. 2004) provided by the MPA-JHU DR7 catalog to estimate the SF-contributed X-ray luminosity. We note that the SFR is based primarily on the Hα emission line, which might be contaminated in the presence of an AGN, but such an effect should lead to an overestimate of the SF-contributed X-ray luminosity, thus strengthening the following conclusion. The information of SFR is available for 137 of the 184 nuclei in the entire sample. Following Hou et al. (2020), we adopt the empirical relation of Ranalli et al. (2003),

$$L^{\rm SF}_{0.5-2} = 4.5 \times 10^{39} \frac{\rm SFR}{M_\odot\ {\rm yr}^{-1}}\ {\rm erg\ s}^{-1}, \quad (1)$$

$$L^{\rm SF}_{2-10} = 5.0 \times 10^{39} \frac{\rm SFR}{M_\odot\ {\rm yr}^{-1}}\ {\rm erg\ s}^{-1}, \quad (2)$$

which has an rms scatter of 0.27 dex and 0.29 dex in the 0.5–2 keV and 2–10 keV band, respectively.

Figure 5 shows the comparison between the measured X-ray luminosity and the empirical X-ray luminosity due to star formation ($L^{\rm SF}_{0.5-2}$, $L^{\rm SF}_{2-10}$) in the two bands. The majority of the detected nuclei lie significantly above the predicted SF-contributed luminosity. This holds in both bands, and more so in the 2–10 keV band. Still, a few SF nuclei (magenta stars) and a few composite nuclei (orange circles) have their X-ray luminosity consistent with the predicted SF luminosity. An X-ray AGN is likely absent or heavily obscured in these nuclei. In the meantime, the majority (but all) of the optically classified AGN (cyan diamonds) lie significantly above the predicted SF luminosity, indicating that an AGN is indeed powering the observed X-ray emission from these objects. Overall, Figure 5 suggests that $L_{2-10} = 10^{41}$ erg s^{-1} can be taken as a practical threshold above which a genuine AGN is present and dominates the X-ray emission. Of the 184 nuclei, 32 have L_{2-10} above this threshold. Additionally, 83 nuclei have their 3σ upper limit above this threshold. We note that only two of the 92 pairs in the current sample (J0907+5203 and J1414-0000, shown as green and yellow crosses in Figure 5) have both nuclei detected above this threshold.

We also test the SF-contributed X-ray luminosity using different relations provided in Lehmer et al. (2010), Mineo

[9] https://wwwmpa.mpa-garching.mpg.de/SDSS/DR7/

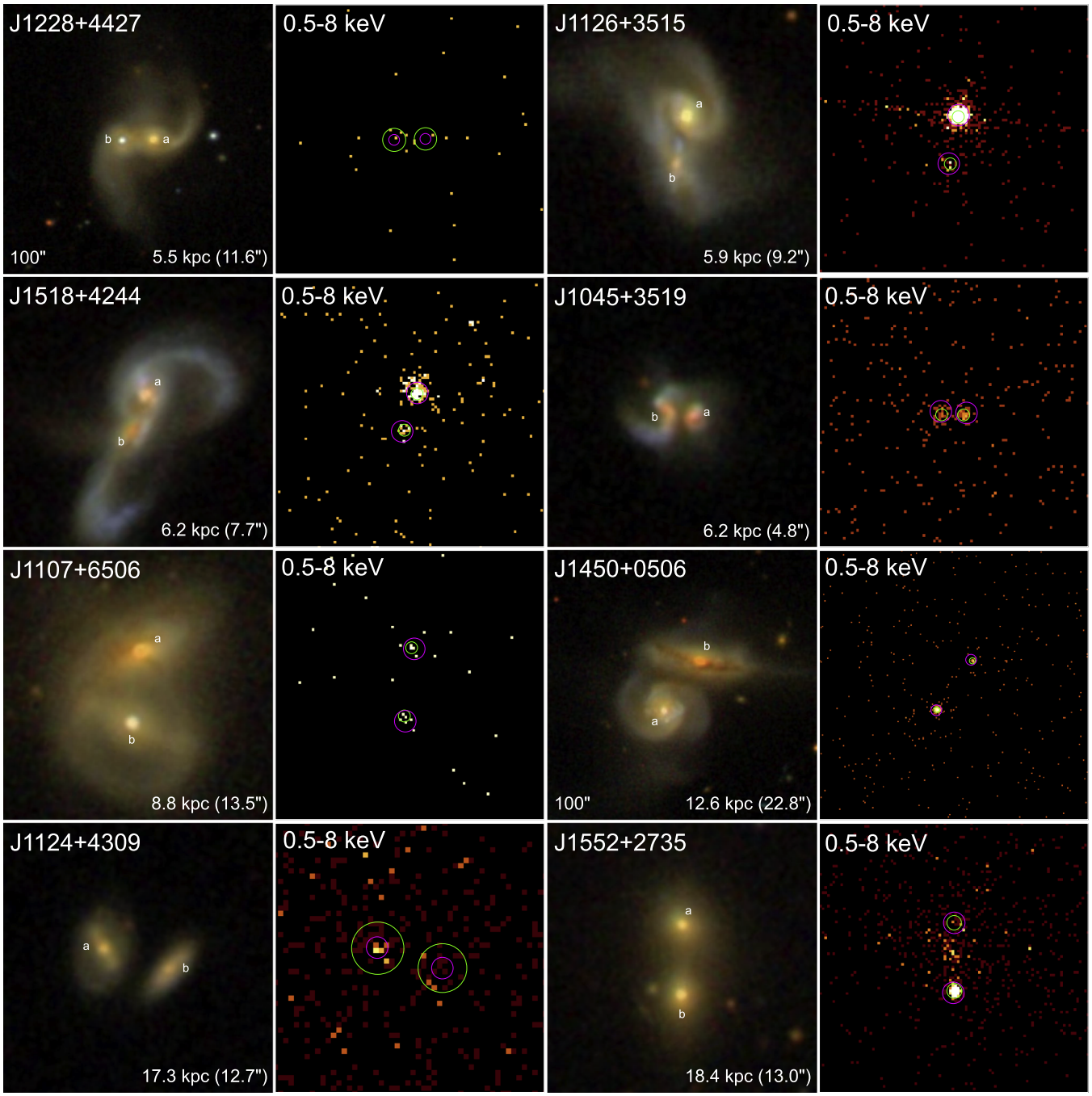

Figure 3. SDSS *gri*-color composite (first and third columns) and Chandra/ACIS 0.5–8 keV (second and fourth columns) images of the eight newly-found close galaxy pairs with both nuclei detected in the X-rays. Each panel has a size of $50'' \times 50''$ unless otherwise labeled. North is up and east is to the left. Magenta circles denote positions of the optical nuclei. Green circles represent the 90% ECR of local PSF.

et al. (2012), and Fragos et al. (2013). The detailed calculation and figures are presented in Appendix. The overall distributions are very similar to that derived in Figure 5, which help to confirm AGNs dominate the X-ray emission for nuclei with $L_{2-10} = 10^{41}$ erg s^{-1}.

4.3. Obscured AGNs Probed by WISE Color and NuSTAR Spectra

The 2–10 keV luminosity, which is derived by assuming a moderate absorption column density $N_{\rm H} = 10^{22}$ cm^{-2}, might be underestimated if the true absorption column density were substantially higher. To check the possibility of a buried but intrinsically luminous AGN, we examine the infrared (IR) color of each galaxy pair provided by the Wide-field Infrared Survey Explorer (WISE) survey Wright et al. (2010). Specifically, we adopt the color of $W1$ (3.4 μm) $-$ $W2$ (4.6 μm), which is sensitive to the presence of a luminous AGN (Jarrett et al. 2011; Stern et al. 2012; Satyapal et al. 2014). Figure 6 plots L_{2-10} versus $W1 - W2$, for both the close galaxy pairs and AGN pairs. Given the relatively large WISE PSF (FWHM $\approx 6''$), the two nuclei in many of these pairs are unresolved and thus share the same value. Nevertheless, this

Table 4
Comparison of X-Ray Detection Rates

Sample (1)	Sample Size (2)	Detection Requirement (3)	No. of Detections (4)	Detection Rate (5)
Nuclei in close pairs	184	$\log L_{2-10} > 41$	32	$18\%^{+3\%}_{-3\%}$
Nuclei with $M_{\rm BH}$	91	$L_{2-10}/L_{\rm Edd} > 10^{-4}$	14	$15\%^{+4\%}_{-5\%}$
Nuclei in H20 AGN pairs (all)	134	$\log L_{2-10} > 41$	36	$27\%^{+5\%}_{-5\%}$
Nuclei in H20 AGN pairs ($r_{\rm p} \lesssim 20$ kpc)	56	$\log L_{2-10} > 41$	22	$39\%^{+10\%}_{-10\%}$
Close pairs	92	at least one detection and $\log L_{2-10} > 41$	30	$32\%^{+7\%}_{-7\%}$
Close pairs	92	dual detection and $\log L_{2-10} > 41$	2	$2\%^{+2\%}_{-2\%}$
Close pairs	92	at least one detection and $\log L_{2-10} > 42$	16	$17\%^{+5\%}_{-5\%}$
Close pairs ($r_{\rm p} < 10$ kpc)	40	at least one detection and $\log L_{2-10} > 41$	17	$41\%^{+12\%}_{-13\%}$
Close pairs ($r_{\rm p} > 10$ kpc)	52	at least one detection and $\log L_{2-10} > 41$	13	$25\%^{+8\%}_{-8\%}$
H20 AGN pairs (all)	67	at least one detection and $\log L_{2-10} > 41$	32	$47\%^{+11\%}_{-10\%}$
H20 AGN pairs ($r_{\rm p} \lesssim 20$ kpc)	28	at least one detection and $\log L_{2-10} > 41$	19	$66\%^{+17\%}_{-18\%}$
Close pairs both with $M_{\rm BH}$	26	at least one detection and $L_{2-10}/L_{\rm Edd} > 10^{-4}$	9	$33\%^{+13\%}_{-15\%}$

Note. Quoted errors, at 1σ, take into account the Poisson error associated with both the umerator and denominator.

does not significantly affect our following conclusion, because a luminous AGN, when existed, is expected to dominate the WISE flux.

Figure 6 shows that most nuclei fall on the blue side of $W1 - W2 = 0.5$, an empirical threshold that separates star-forming galaxies from AGNs (Satyapal et al. 2014). On the other hand, nearly all nuclei with $L_{2-10} > 10^{43}$ erg s^{-1} have $W1 - W2 > 0.5$, finding good agreement between the X-ray and IR AGN classifications. A curious exception is the nucleus (J112648.50+351503.2) with the highest L_{2-10} (1.0×10^{43} erg s^{-1}), which has $W1 - W2 \sim 0.37$, but its high X-ray luminosity warrants an AGN classification, This nucleus is likely accompanied by intense IR starlight of the host galaxy. Also remarkable are a handful of nuclei with $W1 - W2 > 0.5$ but also with $L_{2-10} \lesssim 10^{43}$ erg s^{-1}. Some of these nuclei might host a heavily obscured AGN and have their L_{2-10} significantly underestimated. Fortunately, five of these nuclei have an available NuSTAR spectrum (Section 3.3). In four of the five cases (J0841+0102, J1338+4816, J1354+1238, and J1450+0507), the 2–10 keV luminosity converted from the best-fit model to the NuSTAR spectrum is actually two to seven times higher than the default value of L_{2-10} derived from the Chandra data (Table 3; marked by magenta stars in Figure 6). In the remaining case (J1125+5423), the NuSTAR spectrum-based luminosity is actually two times lower, which might reflect intrinsic variability. Nevertheless, the absorption column densities inferred from the NuSTAR spectra are generally moderate, and in all cases lower than 2×10^{23} cm^{-2} (Table 3). This suggests that the L_{2-10} in the other nuclei with $W1 - W2 > 0.5$ but without NuSTAR observations are rather unlikely to have been underestimated by more than a factor of 10.

4.4. Mean X-Ray Luminosity versus Projected Separation

The left panel of Figure 7 shows L_{2-10} (or upper limits for non-detected nuclei) as a function of projected separation $r_{\rm p}$ for the close galaxy pairs. As mentioned in Section 1, $r_{\rm p}$ is taken as a proxy for the merger phase, with the smallest $r_{\rm p}$ (a few kiloparsecs) indicating the late stage of a merge. A substantial scatter in L_{2-10} over nearly five orders of magnitude exists in this plot, reflecting a wide range of AGN activity in these galaxies. Following Hou et al. (2020), we bin the data points (including the upper limits) into several intervals of $r_{\rm p}$ and estimate the mean luminosity of each r_p bin using the Astronomy SURVial Analysis (ASURV; Feigelson & Nelson 1985), a maximum likelihood estimator of the statistical properties of censored data, as is the case here. We have chosen even bins in logarithmic space covering $3.0\,{\rm kpc} \leqslant r_{\rm p} \leqslant 20\,{\rm kpc}$ and ensured that each bin contain at least 10 nuclei to minimize random fluctuation. We note that the main conclusion below is insensitive to the exact choice of bins. The resultant mean 2–10 keV luminosity of the close galaxy sample is shown by large black squares. For comparison, the full AGN pair sample of Hou et al. (2020) is shown by blue circles, which covers a wider range of $r_{\rm p}$ up to 100 kpc. The mean 2–10 keV luminosities of optically selected single AGNs and SFG pairs, taken from Hou et al. (2020) and calculated with ASURV, are also plotted for comparison (green and red horizontal lines).

The two outermost bins ($10\,{\rm kpc} \lesssim r_{\rm p} < 20\,{\rm kpc}$) have a mean L_{2-10} comparable with each other within the statistical uncertainty, which is also comparable to that of optically selected single AGNs ($2.6[\pm 0.6] \times 10^{41}$ erg s^{-1}). This suggests that galaxy interactions have not generally boosted the AGN activity at such intermediate separations, if the mean X-ray luminosity of single AGNs can be taken as the reference level. On the other hand, as noted by Hou et al. (2020) and reiterated here, the AGN pairs at similar $r_{\rm p}$ show a substantially higher mean L_{2-10}. This difference might again be understood as a systematically higher fraction of luminous AGNs in the Hou et al. (2020) sample, which pertains to their optical classification. We note that a handful of nuclei with the lowest L_{2-10} have a value (or upper limit) consistent with the mean of SFG pairs ($1.3[\pm 0.3] \times 10^{40}$ erg s^{-1}), indicating that an AGN is intrinsically weak or absent in these nuclei.

At smaller $r_{\rm p}$, the mean L_{2-10} finds its highest value at the third bin ($6.3\,{\rm kpc} < r_{\rm p} < 9.0\,{\rm kpc}$), which is about an order of magnitude higher than the mean of the two outer bins as well as the mean of single AGNs. The mean L_{2-10} of the second bin is also significantly elevated. This might be understood as a sign of enhanced SMBH accretion due to merger-driven gas inflows. However, it is noteworthy that the four nuclei with the highest luminosities ($L_{2-10} \gtrsim 10^{43}$ erg s^{-1}) were targeted by Chandra because they were known to be luminous in either

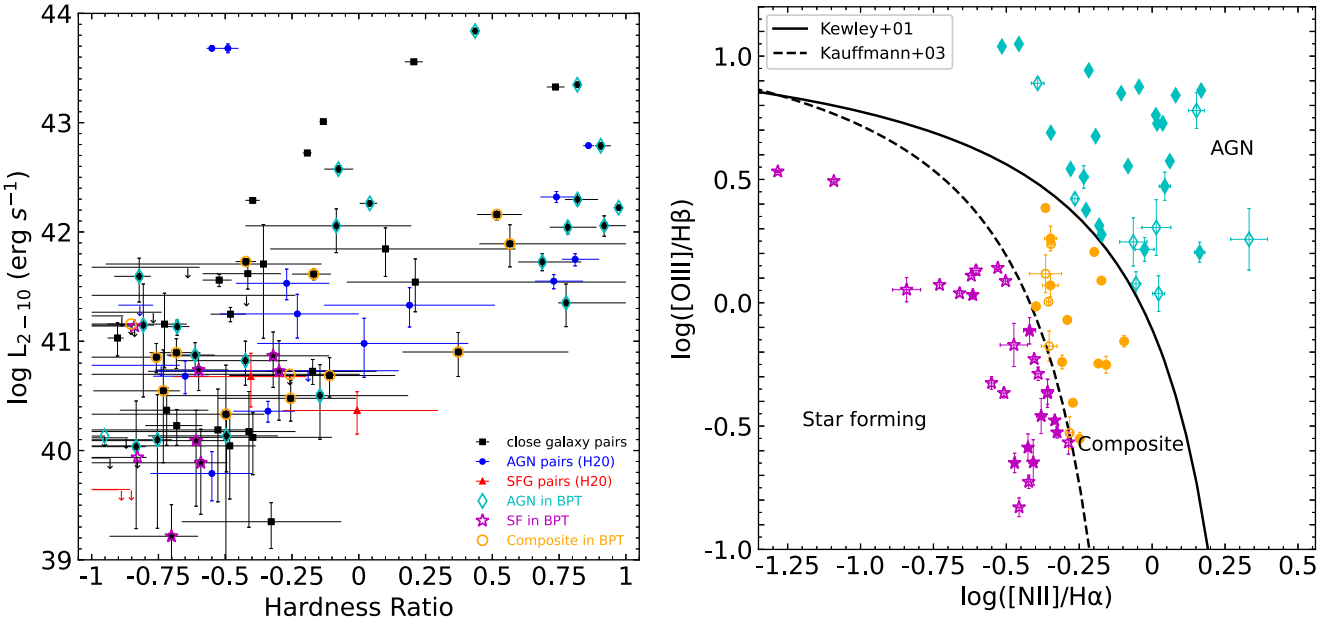

Figure 4. Left: 2–10 keV luminosity vs. hardness ratio. The black squares, blue circles, and red triangles represent X-ray counterparts of close galaxy pairs (current sample), AGN pairs, and SFG pairs (Hou et al. 2020), respectively. Those nuclei undetected in the hard band are marked by arrows. Right: Standard BPT diagram for the nuclei which have reliable optical emission-line measurements (i.e., with a S/N > 3 in each of the four lines). The solid and dashed lines, taken from Kewley et al. (2001) and Kauffmann et al. (2003), define the canonical regions occupied by star-forming nuclei, composite nuclei and AGNs, which are marked by the cyan diamonds, orange circles, and magenta stars, respectively (same in the left panel). Filled and open symbols represent X-ray detected and non-detected nuclei, respectively.

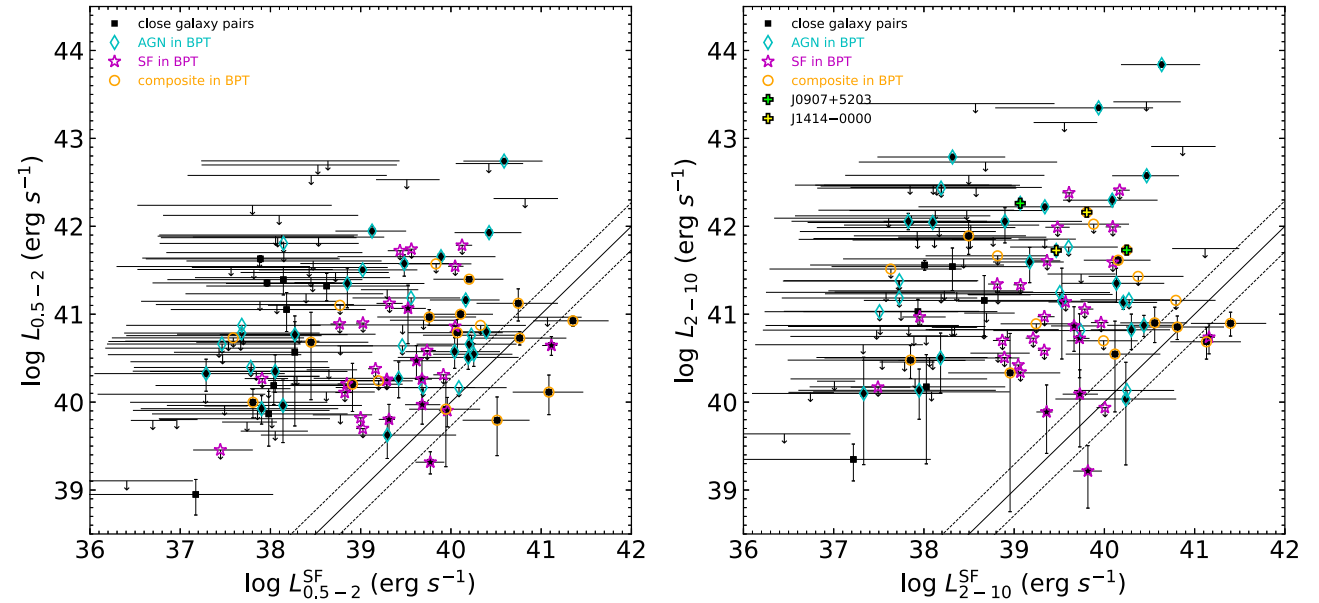

Figure 5. 0.5–2 keV (left panel) and 2–10 keV (right panel) luminosity vs. the predicted luminosity due to star-formation activity. The black squares represent X-ray counterparts of the close galaxy pairs. Those nuclei undetected in a given band are marked by arrows. The black solid line indicates a 1:1 relation, with the pair of dashed lines representing the rms scatter (Equations (1) and (2)). The cyan diamonds, magenta stars, and orange circles denote the optically classified AGNs, SF nuclei, and composite nuclei, respectively. The two pairs with both nuclei detected above $L_{2-10} = 10^{41}$ erg s^{-1} are labeled as green and yellow crosses in the right panel.

hard X-rays or the IR, which potentially introduces a selection effect. We find that removing these nuclei from the second and third r_p bins results in a mean L_{2-10} much closer to the mean of single AGNs. Therefore it remains inclusive whether the upward rising trend between the fourth and third bins is intrinsic. More surprisingly, the mean L_{2-10} continues to decrease toward the smallest r_p. Nine of the 10 nuclei in the innermost bin, in fact, have L_{2-10} (or upper limit) below the mean value of single AGNs. Overall, L_{2-10}–r_p relation suggests little evidence for merger-induced AGN activity in close galaxy pairs.

This is reinforced when the absolute X-ray luminosity is replaced by the X-ray Eddington ratio (L_{2-10}/L_{Edd}), as shown in the right panel of Figure 7. Here L_{Edd} is the Eddington luminosity, which scales with an estimated black hole mass (M_{BH}) based on the stellar velocity dispersion (σ^*) from the

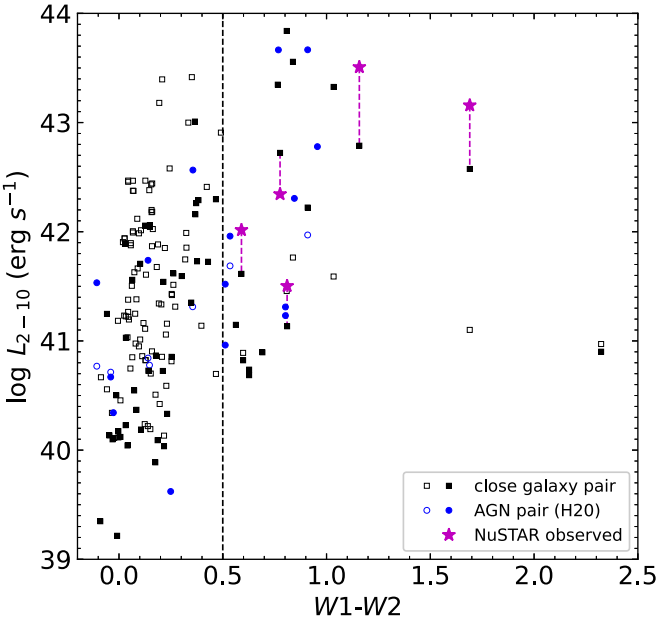

Figure 6. 2–10 keV luminosity vs. $W1 - W2$ color. The close galaxy pairs and AGN pairs of Hou et al. (2020) are shown by black squares and blue circles, respectively. The solid and open symbols represent detections and non-detections. Error bars are neglected for clarity. The magenta stars mark the 2–10 keV luminosity derived from NuSTAR spectra, which are available for five pairs.

MPA-JHU catalog and the empirical $M_{\rm BH}$–σ^* relation from Gültekin et al. (2009). To ensure a reasonable estimate of $M_{\rm BH}$, we have discarded those nuclei with values lower than $10^5\,M_\odot$ or higher than 10% of the host galaxy mass. In total, 91 nuclei have a reliable $M_{\rm BH}$ and appear in the $L_{2-10}/L_{\rm Edd}$–$r_{\rm p}$ plot. We note that two of the four nuclei with $L_{2-10} > 10^{43}$ erg s^{-1} are thus not included. The mean $L_{2-10}/L_{\rm Edd}$ of the Hou et al. (2020) AGN pairs are plotted for comparison, as well as the mean $L_{2-10}/L_{\rm Edd}$ of the single AGNs derived in a similar way. Clearly, the mean $L_{2-10}/L_{\rm Edd}$ of the close galaxy pairs shows no significant enhancement relative to that of single AGNs at any $r_{\rm p}$ bin.

5. Summary and Discussion

In this work, we have presented the detection and statistical analyses of X-ray nuclei in a newly compiled sample of 92 close galaxy pairs at low redshift ($\bar{z} \sim 0.07$), based on archival Chandra observations. The sample is designed to have projected separations $\lesssim$20 kpc and thus representative of the intermediate-to-late stage of galaxy mergers. Also by design, the sample requires no optical emission-line classification of the nuclei, thus it is largely (but not completely) free of selection bias for or against intrinsic AGN activity. This sample has similar X-ray detection sensitivity (down to a limiting luminosity of $\sim 10^{40}$ erg s^{-1}), redshift, and host galaxy mass (Figure 1) compared to the close AGN pairs studied by Hou et al. (2020), but is a factor of about two larger in size, helping to relieve concern about a small number statistics. These factors together offer an unprecedented opportunity for probing the connection between galaxy interaction and AGN activity through nuclear X-ray emission, which is generally thought to be a robust diagnostic of AGNs.

Despite the excellent sensitivity achieved, less than half of the 184 nuclei are firmly detected in the X-rays, among which only four have a 2–10 keV unabsorbed luminosity $\gtrsim 10^{43}$ erg s^{-1}, a conventional threshold for luminous AGNs. Nevertheless, the majority of the nuclei have an X-ray luminosity (or an upper limit in the case of non-detection) significantly above the empirical luminosity due to star-forming activity (Figure 5). This suggests that a weakly accreting SMBH, rather than star formation, is responsible for the observed X-ray emission in most nuclei. Optical line ratios, which are available for 75 nuclei, support this view (Figure 4).

We examine whether the X-ray-detection/non-detections are related to the host galaxy properties. By comparing the distributions of redshift, r-band absolute magnitude of the host galaxy, and X-ray detection limit, between the detected and non-detected nuclei, we find that none of these parameters is statistically distinct between the detected and non-detected nuclei. Our visual examination also does not reveal systematic differences in the global morphology (e.g., more disk-dominated) between the detected and undetected subsets. In Figure 8, we further compare the distributions of stellar velocity dispersion (left panel) and SFR (right panel) between the X-ray detected (red histogram) and undetected nuclei (black histogram). The two subsets both show a large scatter in their stellar velocity dispersion, but there is no systematic difference between the two. This indicates that the detected nuclei are not preferentially found in galaxies with a more massive SMBH (assuming that $M_{\rm BH}$ is statistically reflected by the stellar velocity dispersion). On the other hand, a larger fraction of high SFR ($\gtrsim 0.1\,M_\odot\,{\rm yr}^{-1}$) is found with the detected subset, although, as previously noted, the presence of an AGN may cause an overestimate of the SFR. Neglecting this caveat, such a trend might be taken as evidence that a larger amount of fuel is available in the detected subset for both star formation and SMBH accretion.

We also examine the relation between stellar mass ratio of the pairs and the observed X-ray luminosity. Only about half galaxy pairs (45/92) have reliable stellar mass measurement for both nuclei. Among them, only 27 galaxy pairs have at least one X-ray detected nucleus, which is only a small fraction compared to the whole sample. There is a tentative trend that the more massive galaxy in a pair is more likely to host a more luminous AGN.

Since essentially all nuclei have an SF-contributed luminosity below $L_{2-10} = 10^{41}$ erg s^{-1} (Figure 5), it is practical to adopt this as the threshold, above which a genuine AGN can be identified. This allows us to derive the fraction of pairs containing at least one X-ray-detected nucleus (the case of only one detected nucleus is sometimes referred to as an "offset AGN"), which is ∼33% (Section 4.1). Raising the threshold to 10^{42} erg s^{-1} or restricting to dual AGNs (i.e., both nuclei detected) results in a fraction of $17\%^{+5\%}_{-5\%}$ and $2\%^{+2\%}_{-2\%}$, respectively. These may serve as a useful point of reference for theoretical and numerical studies of AGN triggering in interacting galaxy pairs, by virtue of our sample being largely unbiased to AGN selection. Applying different definitions of AGNs (e.g., based on a threshold of bolometric luminosity, X-ray luminosity, or Eddington ratio), existing numerical studies, including both idealized galaxy merger simulations (e.g., Capelo et al. 2015; Capelo & Dotti 2017; Solanes et al. 2019) and cosmological simulations (e.g., EAGLE, Rosas-Guevara et al. 2019; ASTRID, Chen et al. 2023), typically predict a dual-AGN fraction of few percent for luminous AGNs or accretion rates close to the Eddington limit. This is

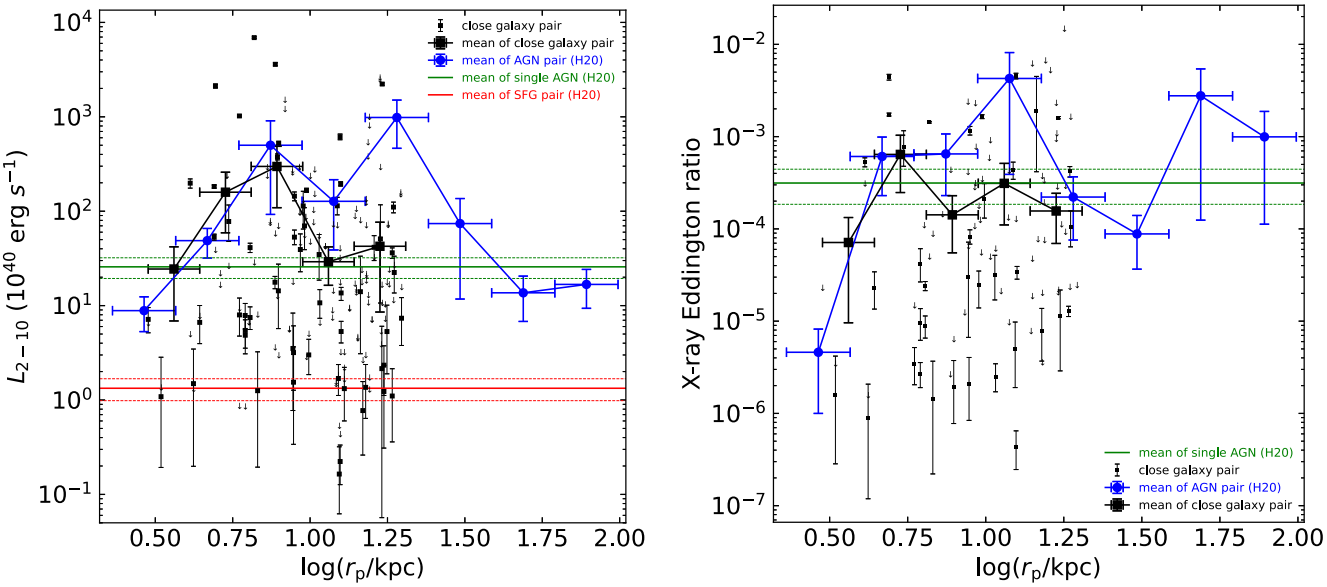

Figure 7. Left: 2–10 keV luminosity as a function of projected separation. The small black squares and blue circles represent close galaxy pairs and the Hou et al. (2020) AGN pairs, respectively. The 3σ upper limit of undetected nuclei are shown by arrows. For each r_p bin, the mean luminosities of close galaxy pairs and the Hou et al. (2020) AGN pairs are represented by the large black squares and blue circles, respectively. The mean value of single AGNs (star-forming galaxy pairs) from Hou et al. (2020) is shown by the green (red) horizontal solid line, with 1σ error bars represented by the dashed green (red) lines. Right: Similar to the left panel, but for the X-ray Eddington ratio. The same r_p bins as in the left panel are adopted. Only those nuclei with a reliable black hole mass estimate (Table 1) are included.

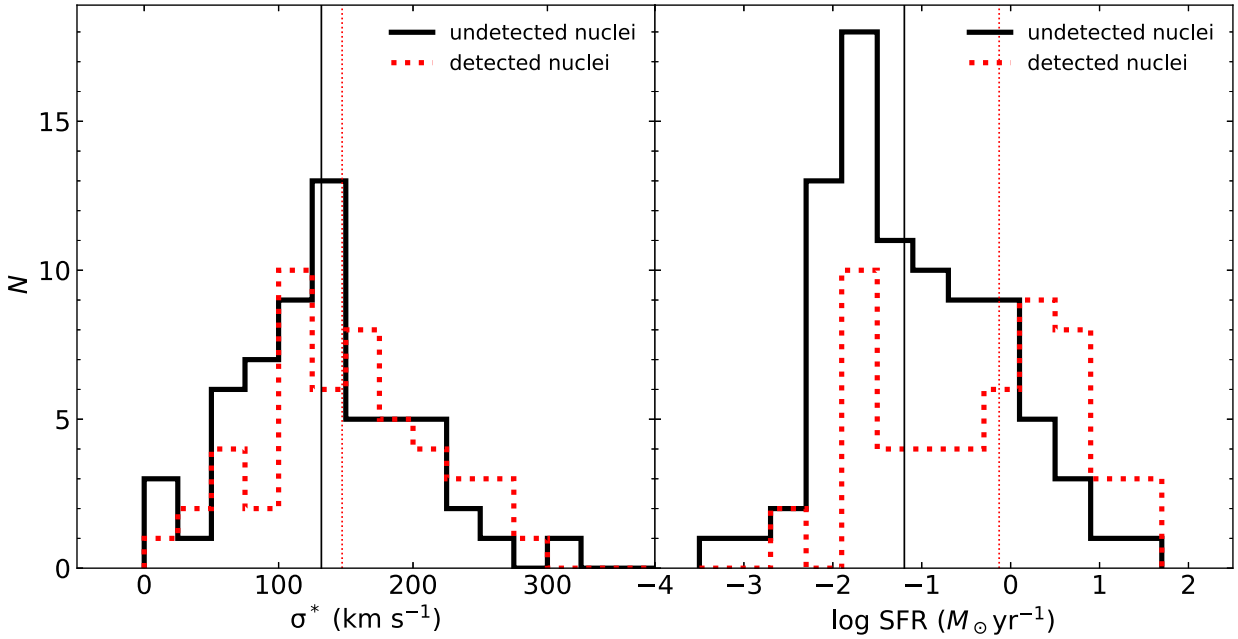

Figure 8. Stellar velocity dispersion (left panel) and star-formation rate (right panel) distributions of the X-ray detected (red histogram) and undetected nuclei (black histogram). The vertical lines mark the median values.

compatible with the above statistics. However, it is noteworthy that current simulations still lack the ability of self-consistently determining the accretion rate and the accretion-induced X-ray luminosity, owing primarily to the lack of resolutions down to the sphere of gravitational influence of the SMBH. This is further complicated by the uncertain degree of circumnulear obscuration. Hence caution is warranted when comparing the observed and predicted AGN fractions.

Hou et al. (2020) revealed a rather surprising trend of decreasing mean X-ray luminosity with decreasing projected separation in their AGN pairs with $r_p \lesssim 10$ kpc. This is reproduced in Figure 7 and further confirmed with the current sample of close galaxy pairs, although one should bear in mind that the innermost bins are driven by a relatively small number of nuclei. Indeed the mean luminosity of the innermost r_p bin is fully consistent with the mean of optically classified single AGNs. The fraction of nuclei with $L_{2-10} > 10^{41}$ erg s^{-1}, $18\% \pm 3\%$ (Table 4), is even marginally lower than that of the single AGNs ($24\% \pm 5\%$; Hou et al. 2020). At face value, this suggests that close galaxy interactions do not *effectively* result in boosted AGN activity, which is contradictive with the general prediction of the aforementioned numerical simulations, in which tidal torques become stronger at the smaller

separations and thus more effective in driving gas to the vicinity of the SMBH. Interestingly, a recent study by Jin et al. (2021) based on SDSS/MaNGA integral-field spectroscopic mapping of low-z galaxies, also found no significant excess in the AGN fraction in any merger phase compared to that of isolated galaxies. The galaxy pair sample of Jin et al. (2021) is free of pre-selection of AGN characteristics, which is similar to ours.

Two physical scenarios were proposed by Hou et al. (2020) to explain the behavior revealed in Figure 7, which we elaborate here. The first is an obscuration effect. In close galaxy pairs, gravitational perturbation can be sufficiently strong to induce gas inflows in one or both galaxies, which in turn result in the accumulation of circumnuclear cold gas that heavily obscures even the hard X-rays, regardless of the intrinsic AGN luminosity. Indeed, observational evidence has been gathered for heavily obscured AGN pairs at kiloparsec separations (Satyapal et al. 2017; Pfeifle et al. 2019; De Rosa et al. 2023). However, obscuration cannot be the sole cause of the low-to-moderate luminosities observed in most nuclei of our sample, in view of the following countering evidences. On the one hand, in the five nuclei with a high-quality NuSTAR spectrum, the best-fit foreground absorption column densities (Table 3) are far below that required ($\gtrsim 10^{24}$ cm^{-2}) to completely block X-ray photons below a few kilo electron volts. On the other hand, in a recent attempt of directly detecting circumnuclear cold gas in seven pairs of dual-AGNs based on high-resolution CO observations, Hou et al. (2023) found no evidence for an equivalent hydrogen column density $\gtrsim 10^{24}$ cm^{-2} in any of the 14 nuclei, which are all included in Hou et al. (2020; 10 included in the current sample). Nevertheless, it remains interesting to see whether a dense circumnuclear gas exists in the several nuclei with the smallest $r_{\rm p}$ ($\lesssim$5 kpc), which also have the lowest apparent L_{2-10}, through higher resolution CO observations and hard X-ray observations.

In the second scenario, most SMBHs in the close galaxy pairs are currently weakly accreting, which is the result of *negative* AGN feedback that have expelled the circumnuclear gas and prevents the SMBH from maintaining a high level of accretion. Numerical simulations of idealized galaxy mergers suggest that gas inflows may start as soon as the first pericentric passage of the two galaxies, typically at a physical separation of $\gtrsim$10 kpc, while substantial enhancement of SMBH accretion may not occur until shortly after the second pericentric passage, which lasts for a few tens of megayears (Capelo et al. 2015). At and after this stage, the separation of the two nuclei remain at no more than 10 kpc, which is consistent with the inner bins in Figure 7. An efficient feedback can explain the moderate column densities inferred for at least a subset of the nuclei. The feedback is likely in a kinetic mode mediated by jets and winds (Yuan & Narayan 2014), given that most nuclei have a low Eddington ratio (Figure 7). Future high-resolution radio and optical spectroscopic observations will be crucial to search for direct evidence of this feedback in the close galaxy pairs.

M.H. is supported by the National Natural Science Foundation of China (12203001) and National Postdoctoral Program for Innovative Talents of China Postdoctoral Science Foundation (grant BX2021016). H.L. and Z.L. acknowledge support by the National Natural Science Foundation of China (12225302). S.F. acknowledges support from National Natural Science Foundation of China (No. 12103017) and Natural Science Foundation of Hebei Province (No. A2021205001). X. L. acknowledges support from NSF grants AST-2108162 and AST-2206499. The authors wish to thank Drs. Yanmei Chen and Zongnan Li for helpful discussions.

Appendix
Comparison of Star Formation Contribution to X-Ray Luminosity

Lehmer et al. (2010) calibrated the 2–10 keV X-ray emission from both high- and low-mass X-ray binaries (HMXBs and LMXBs) based on a sample of 17 luminous infrared galaxies and presented an empirical correlation between 2 to 10 keV luminosity $L_{\rm HX}^{\rm gal}$, SFR, and stellar mass as

$$L_{\rm HX}^{\rm gal} = \alpha M_{*} + \beta {\rm SFR}, \tag{A1}$$

where $\alpha = (9.05 \pm 0.37) \times 10^{28}$ erg s^{-1} $M_{\odot}^{-1}$ and $\beta = (1.62 \pm 0.22) \times 10^{39}$ erg s^{-1} $(M_{\odot}$ yr$^{-1})^{-1}$. As estimated based on SDSS images, we adopted a uniform factor of 20% for the contribution from LMXBs to enclose the stellar mass in the nuclear region ($\sim 2''$). Since only half of the galaxies have stellar mass measurement, the data points are reduced compared to the others (Figure 9, left panel). This relation

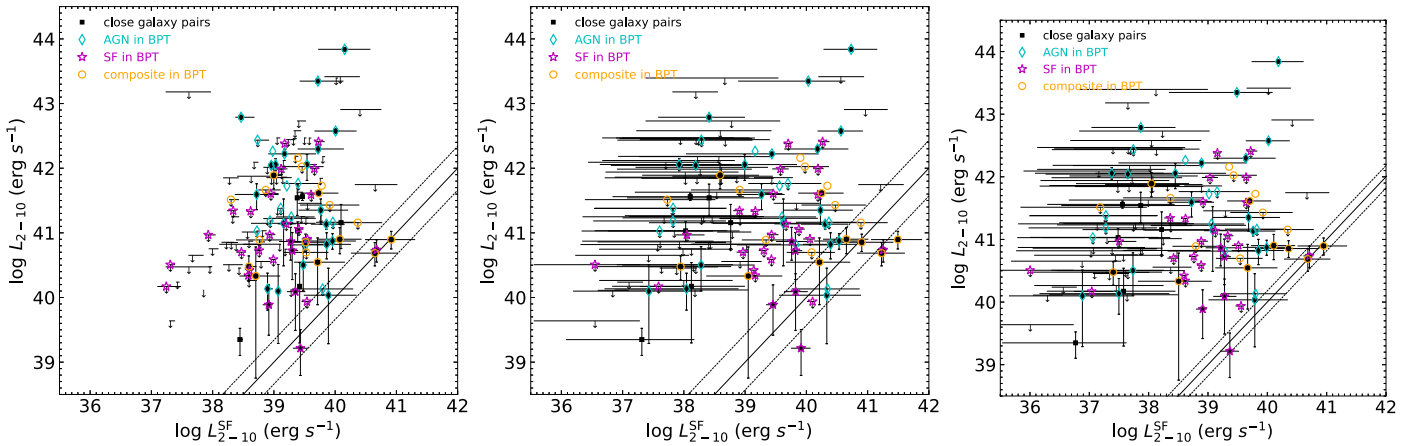

Figure 9. 2–10 keV luminosity vs. the predicted luminosity due to star-formation activity according to the relation in Lehmer et al. (2010; left panel), Mineo et al. (2012; middle panel), and Fragos et al. (2013; right panel), respectively. The black squares represent X-ray counterparts of the close galaxy pairs. Those nuclei undetected in a given band are marked by arrows. The black solid line indicates a 1:1 relation, with the pair of dashed lines representing the rms scatter. The cyan diamonds, magenta stars and orange circles denote the optically classified AGNs, SF nuclei and composite nuclei, respectively.

gives a bit higher 2–10 keV X-ray luminosity because it slightly overestimates the contribution from the pure star-formation-related processes. However, nearly all nuclei still lie significantly above the predicted luminosity.

Mineo et al. (2012) considers X-ray emission only from HMXBs with the contamination from LMXBs carefully subtracted based on a sample of 29 nearby star-forming galaxies. But the predicted SF-contributed luminosity is given in 0.5–8 keV as

$$L_{0.5-8\ \mathrm{keV}}^{\mathrm{XRB}}(\mathrm{erg\ s^{-1}}) = 2.61 \times 10^{39}\ \mathrm{SFR}\ (M_{\odot}\ \mathrm{yr^{-1}}). \quad \text{(A2)}$$

So we multiply a conversion factor to calculate the 2–10 keV luminosity. As shown in Figure 9 (middle panel), the distribution is basically the same as that derived in Figure 5.

The relations in Fragos et al. (2013) are derived from large-scale population synthesis simulations. The X-ray contribution from star-formation-related processes are estimated from HMXBs with a dependence on the mean metallicity, given by

$$\log(L_{\mathrm{X}}/\mathrm{SFR}) = \beta_0 + \beta_1 Z + \beta_2 Z^2 + \beta_3 Z^3 + \beta_4 Z^4, \quad \text{(A3)}$$

where $\beta_0 = 42.28 \pm 0.02$, $\beta_1 = -62.12 \pm 1.32$, $\beta_2 = 569.44 \pm 13.71$, $\beta_3 = -1833.80 \pm 52.14$, and $\beta_4 = 1968.33 \pm 66.27$. We assume a solar metallicity. The distribution (Figure 9, right panel) is also very similar to that derived Figure 5, where the majority of the nuclei lie above the predicted SF-contributed luminosity.

ORCID iDs

Lin He https://orcid.org/0000-0002-7875-9733
Meicun Hou https://orcid.org/0000-0001-9062-8309
Zhiyuan Li https://orcid.org/0000-0003-0355-6437
Shuai Feng https://orcid.org/0000-0002-9767-9237
Xin Liu https://orcid.org/0000-0003-0049-5210

References

Abazajian, K. N., Adelman-McCarthy, J. K., Agüeros, M. A., et al. 2009, ApJS, 182, 543
Baldry, I. K., Liske, J., Brown, M. J. I., et al. 2018, MNRAS, 474, 3875
Baldwin, J. A., Phillips, M. M., & Terlevich, R. 1981, PASP, 93, 5
Barnes, J. E., & Hernquist, L. 1992, ARA&A, 30, 705
Brightman, M., Baloković, M., Koss, M., et al. 2018, ApJ, 867, 110
Brinchmann, J., Charlot, S., White, S. D. M., et al. 2004, MNRAS, 351, 1151
Capelo, P. R., & Dotti, M. 2017, MNRAS, 465, 2643
Capelo, P. R., Volonteri, M., Dotti, M., et al. 2015, MNRAS, 447, 2123
Chen, N., Di Matteo, T., Ni, Y., et al. 2023, MNRAS, 522, 1895
Comerford, J. M., Pooley, D., Gerke, B. F., & Madejski, G. M. 2011, ApJL, 737, L19
De Rosa, A., Vignali, C., Severgnini, P., et al. 2023, MNRAS, 519, 5149
De Rosa, A., Vignali, C., Bogdanović, T., et al. 2019, NewAR, 86, 101525
Di Matteo, T., Springel, V., & Hernquist, L. 2005, Natur, 433, 604
Feigelson, E. D., & Nelson, P. I. 1985, ApJ, 293, 192
Feng, S., Shen, S.-Y., Yuan, F.-T., et al. 2019, ApJ, 880, 114
Foord, A., Gültekin, K., Nevin, R., et al. 2020, ApJ, 892, 29
Fragos, T., Lehmer, B., Tremmel, M., et al. 2013, ApJ, 764, 41
Fu, H., Myers, A. D., Djorgovski, S. G., et al. 2015a, ApJ, 799, 72
Fu, H., Wrobel, J. M., Myers, A. D., Djorgovski, S. G., & Yan, L. 2015b, ApJL, 815, L6
Gross, A. C., Fu, H., Myers, A. D., Wrobel, J. M., & Djorgovski, S. G. 2019, ApJ, 883, 50
Gültekin, K., Cackett, E. M., Miller, J. M., et al. 2009, ApJ, 706, 404
Hou, M., Li, Z., & Liu, X. 2020, ApJ, 900, 79
Hou, M., Liu, X., Guo, H., et al. 2019, ApJ, 882, 41
Hou, M., Li, Z., Liu, X., et al. 2023, ApJ, 943, 5050
Jarrett, T. H., Cohen, M., Masci, F., et al. 2011, ApJ, 735, 112
Jin, G., Dai, Y. S., Pan, H.-A., et al. 2021, ApJ, 923, 6
Kashyap, V. L., van Dyk, D. A., Connors, A., et al. 2010, ApJ, 719, 900
Kauffmann, G., Heckman, T. M., Tremonti, C., et al. 2003, MNRAS, 346, 1055
Kewley, L. J., Dopita, M. A., Sutherland, R. S., Heisler, C. A., & Trevena, J. 2001, ApJ, 556, 121
Koss, M., Mushotzky, R., Treister, E., et al. 2012, ApJL, 746, L22
Lehmer, B. D., Alexander, D. M., Bauer, F. E., et al. 2010, ApJ, 724, 559
Liu, X., Civano, F., Shen, Y., et al. 2013, ApJ, 762, 110
Liu, X., Greene, J. E., Shen, Y., & Strauss, M. A. 2010, ApJL, 715, L30
Liu, X., Shen, Y., Strauss, M. A., & Hao, L. 2011, ApJ, 737, 101
Luo, A. L., Zhao, Y.-H., Zhao, G., et al. 2015, RAA, 15, 1095
Merritt, D., & Milosavljević, M. 2005, LRR, 8, 8
Mineo, S., Gilfanov, M., & Sunyaev, R. 2012, MNRAS, 419, 2095
Park, T., Kashyap, V. L., Siemiginowska, A., et al. 2006, ApJ, 652, 610
Pfeifle, R. W., Satyapal, S., Secrest, N. J., et al. 2019, ApJ, 875, 117
Ranalli, P., Comastri, A., & Setti, G. 2003, A&A, 399, 39
Rosas-Guevara, Y. M., Bower, R. G., McAlpine, S., Bonoli, S., & Tissera, P. B. 2019, MNRAS, 483, 2712
Satyapal, S., Ellison, S. L., McAlpine, W., et al. 2014, MNRAS, 441, 1297
Satyapal, S., Secrest, N. J., Ricci, C., et al. 2017, ApJ, 848, 126
Shen, S.-Y., Argudo-Fernández, M., Chen, L., et al. 2016, RAA, 16, 43
Silverman, J. D., Kampczyk, P., Jahnke, K., et al. 2011, ApJ, 743, 2
Solanes, J. M., Perea, J. D., Valentí-Rojas, G., et al. 2019, A&A, 624, A86
Stern, D., Assef, R. J., Benford, D. J., et al. 2012, ApJ, 753, 30
Teng, S. H., Schawinski, K., Urry, C. M., et al. 2012, ApJ, 753, 165
Toomre, A., & Toomre, J. 1972, ApJ, 178, 623
Wang, J.-M., Chen, Y.-M., Hu, C., et al. 2009, ApJL, 705, L76
Wik, D. R., Hornstrup, A., Molendi, S., et al. 2014, ApJ, 792, 48
Winter, L. M., Mushotzky, R. F., Reynolds, C. S., & Tueller, J. 2009, ApJ, 690, 1322
Wright, E. L., Eisenhardt, P. R. M., Mainzer, A. K., et al. 2010, AJ, 140, 1868
Yuan, F., & Narayan, R. 2014, ARA&A, 52, 529
Zappacosta, L., Comastri, A., Civano, F., et al. 2018, ApJ, 854, 33